Monthly Notices of the ROYAL ASTRONOMICAL SOCIETY

MNRAS **553,** 1–19 (2026)
Advance Access publication 2026 October 14

https://doi.org/10.1093/mnras/stag1951

The physical and chemical structure of Titan's upper atmosphere: energy balance, photochemistry, and Jeans escape

Sudeshna Boro Saikia [1]★ Jonathan Tennyson [2] Shuchen Ji,[2] Nils-Martin Robeling,[1] Ivan Stanković,[1] Gwenaëlle Van Looveren [1] Simon Schleich,[1] Colin P. Johnstone,[3] Kristina G. Kislyakova[1] and Manuel Güdel[1]

[1]*Department of Astrophysics, University of Vienna, Türkenschanzstrasse 17, A-1180 Vienna, Austria*
[2]*Department of Physics and Astronomy, University College London, London WC1E 6BT, UK*
[3]*International Institute for Applied Systems Analysis, Schloßplatz 1, A-2361 Laxenburg, Austria*

Accepted 2026 October 5. Received 2026 September 9; in original form 2026 July 7

ABSTRACT

Titan's upper atmospheric layers provide a unique opportunity to study how photochemistry, photoionization, haze microphysics, and escape processes shape its atmospheric chemical structure, providing a unique benchmark for understanding these processes in exoplanets. Using a 1D first-principles approach, we extend the Kompot model to simulate Titan's upper atmosphere and investigate its thermal and chemical structure, and Jeans escape. We performed self-consistent simulations of Titan's upper atmosphere, above the dense haze layer, over a 1D radial grid by solving the coupled hydrodynamics, thermal and photochemical kinetic, and energy balance equations. We considered heating by stellar X-ray and ultraviolet (XUV) and infrared radiation, and cooling due to radiative emission of methane (CH_4) and hydrogen cyanide (HCN). We also included additional 19 photochemical and 117 thermal reactions to Kompot's standard chemical network. Our modelled atmospheric temperature structures lie within the observed variability of Titan's atmospheric temperature profile. Our simulations reproduce observed nitrogen (N_2) and CH_4 densities in the upper atmosphere, and abundance of minor chemical species also broadly agree with observationally derived abundances. Near the exobase, our CH_4 mixing ratio overlaps with Cassini–Huygens results, and our model H_2 mixing ratios also exhibit broad agreement with observations. Our simulations suggest no significant thermal loss of CH_4, even under the conditions of an early Sun's XUV environment.

Key words: planets and satellites: atmospheres – planets and satellites: individual.

1 INTRODUCTION

Titan, Saturn's largest moon, provides a unique laboratory to study how nitrogen (N_2)-dominated atmospheres originate and evolve under conditions vastly different from Earth's. Furthermore, the co-existence of methane (CH_4) with N_2 makes it a compelling natural laboratory to study atmospheric disequilibrium processes, such as photochemistry, photoionization, and photochemically produced aerosols known as hazes. The cascade of chemical reactions associated with these disequilibrium processes leads to the production of complex organic compounds in Titan's atmosphere. Outside the Solar system, evidence of such atmospheric disequilibrium (S.-M. Tsai et al. 2023; T. G. Beatty et al. 2024; A. Y. Jaziri et al. 2025) and detection of atmospheric CH_4 (G. Guilluy et al. 2022; N. Madhusudhan et al. 2023; J. Taylor 2025) have been only reported in hydrogen-rich massive exoplanets. No clear evidence of an atmosphere rich in N_2 or CH_4 has been detected around smaller exoplanets (e.g. S. Zieba et al. 2023; Q. Xue et al. 2025). However, the wide diversity of exoplanets observed by the *James Webb Space Telescope* (*JWST*), and upcoming next-generation instruments make CH_4 and other hydrocarbon discovery in a widely diverse population of exoplanets a near-future reality. Robust interpretation of such discoveries would require an understanding of how various physical and chemical processes shape the atmospheric chemical and thermal profiles and observable signatures of Titan, the best example in the Solar system of an N_2- and CH_4-rich atmosphere in disequilibrium.

While the exact origin of Titan's present-day atmospheric composition is debated, formation of N_2 via photolysis of ammonia (NH_3) and outgassing of CH_4 are considered to be the most likely mechanisms (G. Tobie, J. I. Lunine & C. Sotin 2006; S. M. Hörst 2017). Observations taken by the Cassini–Huygens mission and ground-based instruments such as Atacama Large Millimeter Array (ALMA) have revealed its rich atmospheric chemistry, which includes molecular hydrogen, noble gases, hydrocarbons, cyanides, and oxygen-bearing species (C. A. Nixon 2024, and references therein). Many of these chemical species form precursors to Titan's organic haze, which plays an important role in Titan's

★ E-mail: sudeshna.boro.saikia@univie.ac.atIt

© The Author(s) 2026.
Published by Oxford University Press on behalf of Royal Astronomical Society. This is an Open Access article distributed under the terms of the Creative Commons Attribution License (https://creativecommons.org/licenses/by/4.0/), which permits unrestricted reuse, distribution, and reproduction in any medium, provided the original work is properly cited.

Downloaded from academic.oup.com/mnras/article/553/1/stag1951/8916626 by guest on 10 November 2026

atmospheric dynamics and radiative processes (M. G. Tomasko et al. 2005).

Central to Titan's diverse atmospheric chemistry are photodissociation and photoionization driven by the solar high-energy radiation at X-ray and ultraviolet (XUV) wavelengths. Ionization in Titan's atmosphere is also driven by solar energetic particles, cosmic rays, and particles from Saturn's magnetosphere (T. E. Cravens et al. 2009; G. Gronoff et al. 2009). These processes have been studied extensively with photochemical kinetics models. Before Cassini–Huygens, the models were primarily focussed towards neutral chemistry involving CH_4 and N_2 (D. F. Strobel 1974; Y. L. Yung, M. Allen & J. P. Pinto 1984). With the discovery of heavier ions in Titan's upper atmosphere, photochemical models are now expanded to include both ion and neutral chemistry (S. M. Hörst, V. Vuitton & R. V. Yelle 2008; V. A. Krasnopolsky 2014; M. Dobrijevic et al. 2016; V. Vuitton et al. 2019). Some models also explicitly couple photochemical kinetics with haze particle formation, linking gas-phase chemistry with aerosol microphysics (P. Lavvas, A. Coustenis & I. Vardavas 2008a, b; P. Lavvas, R. V. Yelle & V. Vuitton 2009). The chemical abundances derived in these models are generally in good agreement with observations. However, existing models cannot yet explain the observations of complex heavier ions and the high CH_4 and H_2 abundance in Titan's upper thermosphere. These discrepancies are closely tied to limitations in our knowledge of heavier ion chemistry, missing reaction rates, and model sensitivity to the assumed atmospheric thermal profile.

The temperature structure of an atmosphere plays a critical role in shaping its chemical profile by controlling reaction rates, condensation, and escape of atmospheric gases to space. *In situ* measurements taken by the Huygens Atmospheric Structure Instrument (HASI) of Cassini–Huygens, as it landed on Titan's surface, revealed a complex atmospheric temperature structure with multiple temperature inversions (M. Fulchignoni et al. 2005). These measurements are at least a few tens of Kelvin hotter than temperatures derived from *in situ* measurements taken by the Cassini–Huygens' INMS instrument during multiple flybys (D. Snowden et al. 2013) and remote sensing data (E. Lellouch et al. 2019; A. E. Thelen et al. 2022). The observed disagreement between different instruments can be attributed to instrumental sensitivity, seasonal and diurnal variations, and Titan's location within Saturn's magnetosphere (D. Snowden et al. 2013; C. A. Nixon et al. 2025). A range of models have simulated Titan's vertical temperature profile where heating due to solar extreme ultraviolet (EUV) radiation and radiative cooling by molecules are the key mechanisms regulating the temperature structure (R. V. Yelle 1991; I. C. F. Müller-Wodarg et al. 2000; J. M. Bell et al. 2014; D. Snowden & R. V. Yelle 2014). The exact molecules included in the radiative cooling calculations, however, vary from model to model. Effects of aerosol heating and particle precipitation from Saturn's magnetosphere are also considered in some models as additional energy sources (P. Lavvas et al. 2009; D. Snowden & R. V. Yelle 2014).

However, a self-consistent atmospheric model that integrates atmospheric chemistry, temperature structure calculated from first principles, and thermal escape rate has not been applied to study Titan's upper atmosphere. This matters as thermal structure and chemical composition is tightly coupled via radiative heating and cooling, and chemical reaction kinetics, which in turn affects the thermal escape of atmospheric gas and atmospheric evolution. A self-consistent upper atmospheric model could answer some of the outstanding questions on Titan's upper atmospheric temperature structure, chemical composition gradients, atmospheric escape, and long-term evolution. Such a unified self-consistent approach is also critical for exoplanet atmospheres where observations are sparse and limited.

In this work, we update the 1D upper atmospheric model Kompot (C. P. Johnstone et al. 2018), originally developed to study the upper atmospheres of Earth and Venus, to simulate the thermo-chemical structure of Titan's upper atmosphere. model K We include the feedback between chemical reactions and energy balance in our self-consistent model of Titan's upper atmosphere and benchmark our model against remote sensing and *in situ* observations of Titan. We also calculate the Jeans escape rate within our self-consistent simulations. This paper is organized as follows: In Section 2, we provide a general description of the Kompot code, followed by a description of the model updates implemented in this work. The results and discussion are provided in Section 3, and the conclusions are outlined in Section 4.

2 MODEL DESCRIPTION

The simulations presented in this work were carried out with an updated version of the 1D thermo-chemical code Kompot (C. P. Johnstone et al. 2018), as described in the following subsections. The standard Kompot code solves the equations governing hydrodynamics, chemical kinetics, and energy transport across a radial grid to self-consistently calculate the thermal and the chemical profile of planetary upper atmospheres, and the thermal loss of individual chemical species. The lower boundary of the simulation can be arbitrarily set at any altitude in the atmosphere, and the upper boundary lies at the exobase. The lower boundary is usually set above any cloud or haze layers as their effects are currently not included in the model. The gas mixture in the model is split into ions, neutrals, and electrons with their own separate temperatures, and the vertical structure of the atmosphere is calculated as the balance between thermal, chemical, and hydrodynamic processes.

The Kompot code calculates the atmospheric thermal structure by solving the energy equations, which include heating and cooling terms, thermal conduction, and energy exchange between ions, electrons and neutrals. In addition to direct heating by the stellar XUV and infrared (IR) radiation field, the model accounts for electron heating by elastic collisions with nonthermal electrons, exothermic heating, and Joule heating. The cooling is driven by radiative losses by molecules and atoms which include CO_2, H_2O, NO, H_3^+, and O. The chemical profile is calculated using a network of chemical reactions, coupled with advection, and eddy and molecular diffusion. While molecular diffusion is calculated self-consistently, eddy diffusion is treated as a free parameter. The original network consists of 503 chemical reactions containing 63 neutral and 30 ion species. This includes 56 photoreactions and 7 photoelectron reactions.

Within the simulation domain of a Kompot model, the atmosphere expands and contracts in response to the changes in the gas temperature and composition, and the code allows for a dynamic calculation of the exobase. The Jeans escape rate for each species is calculated at the exobase following the prescription of S. J. Bauer & H. Lammer (2004). A full description of the Kompot code, including its validation against Earth and Venus, can be found in C. P. Johnstone et al. (2018). For an additional discussion on the Jeans escape rate, we refer the reader to G. Van Looveren et al. (2024). Kompot has also been applied to

Downloaded from academic.oup.com/mnras/article/553/1/stag1951/8916626 by guest on 10 November 2026

study the hydrodynamic escape of H_2O (C. P. Johnstone 2020) and N_2 (C. P. Johnstone et al. 2019) atmospheres. More recently, we also carried out a grid of Kompot atmospheric simulations to investigate the atmospheric retention of N_2 and CO_2 rich atmospheres on small rocky exoplanets around a diverse stellar population (G. Van Looveren et al. 2024, 2025).

In the following subsections, we describe the model updates carried out in this work, which include extending the energy calculations to include radiative cooling due to CH_4 and HCN, and the chemical network to include nitrile, hydrocarbon and ammonia chemistry. These updates extend the code's applicability to a broader class of planetary atmospheres, including those found on sub-Neptunes and outer Solar system bodies.

2.1 Thermal structure

Thermal emission of CH_4 and HCN plays an important role in determining Titan's atmospheric heat balance (R. V. Yelle 1991; J. M. Bell et al. 2010; L. Rezac et al. 2013). For the CH_4 cooling rate, we consider non-local thermodynamic equilibrium (non-LTE) effects by applying the formalism of R. V. Yelle (1991), where level populations are determined from statistical equilibrium for a selected set of ro-vibrational bands. In addition, we computed the CH_4 cooling rate using a spectroscopic line list under the LTE assumption, for comparison with the band-averaged non-LTE formulation used in the R. V. Yelle (1991) scheme. For HCN, however, we only consider cooling rates calculated under the LTE assumption.

The total non-LTE CH_4 cooling rate, assuming a photon escape probability of 1, is given by

$$Q_{\rm NLTE}(T) = \sum_{i=1}^{4} n_{{\rm u},i} h c \tilde{\nu}_i A_i, \tag{1}$$

where h is the Planck constant in erg s; c is the speed of light in cm s^{-1}; and $n_{{\rm u},i}$, $\tilde{\nu}_i$, and A_i are the population of the upper energy level in cm^{-3}, wave number in cm^{-1}, and Einstein A coefficient in s^{-1}, respectively, for the band i at 7.7, 3.3, 2.3, and 1.7 μm. To estimate the level population $n_{{\rm u},i}$, we follow the two-level approximation

$$n_{{\rm u},i} = n_{\rm CH_4} \frac{C_{{\rm lu},i}}{(C_{\rm ul} + A_i)}, \tag{2}$$

where $n_{\rm CH_4}$ is the number density of CH_4, $C_{\rm ul}$ is the collisional de-excitation rate, and $C_{{\rm lu},i}$ is the collision excitation rate for each band; u stands for the upper and l stands for the lower energy level. The collisional dexcitation rate is related to the de-excitation probability $P_{\rm ul}$ through

$$C_{\rm ul} = n_{\rm N_2} P_{\rm ul} \sigma \sqrt{\frac{8 k_{\rm B} T}{\mu}}, \tag{3}$$

where $n_{\rm N_2}$ is the number density of N_2 in cm^{-3}, σ is the effective collision cross-section in cm^{-2}, $k_{\rm B}$ is the Boltzmann constant in erg K^{-1}, T is the gas temperature in K, and μ is the reduced mass in g. The collisional excitation rate is estimated as follows:

$$C_{{\rm lu},i} = C_{\rm ul} \exp\left(\frac{-h\nu_i}{k_{\rm B} T}\right). \tag{4}$$

In this formulation, each rotational band is represented by a single effective transition with the same de-excitation probability $P_{\rm ul} = 1.4 \times 10^{-6}$ (see tables 1 and 2 in R. V. Yelle 1991). Furthermore, the statistical weights for the upper and lower levels are considered to be identical. Including a more extensive statistical equilibrium calculation for the level population $n_{\rm u}$ is currently not feasible, as it requires collision rate data for all vibrational-rotational levels with different atmospheric constituents (e.g. N_2, H_2, and e$^-$), which are largely unavailable in current data bases. Hence, we adopt the approximation of R. V. Yelle (1991) to account for non-LTE CH_4 cooling due to collisions with N_2, the dominant atmospheric gas in Titan, and compare the results against the LTE calculation described below.

To determine the LTE cooling rate of CH_4 and HCN, we use the approach of J. Tennyson et al. (2016) and calculate the cooling rate per molecule, $\Lambda(T)$ in units of erg s^{-1} sr^{-1} molecule^{-1}:

$$\Lambda(T) = \frac{1}{4\pi Z(T)} \sum_{i,j} A_{ij}\, h\, c\, \tilde{\nu}_{ij}\, g_i \exp\left(\frac{-c_2 E_i}{T}\right), \tag{5}$$

where $Z(T)$ is the partition function, the sum is over all transitions with i and j being the upper and lower states of each transition, respectively, A_{ij} is the Einstein A coefficient (s^{-1}), $h = 6.626 \times 10^{-27}$ erg s is the Planck's constant, c is the speed of light in cm s^{-1}, $\tilde{\nu}_{ij}$ is the wave number of the emitted photon in cm^{-1}, g_i is the total state degeneracy, $c_2 = 1.438\,777\,36$ cm K is the second radiation constant, E_i is the energy of state i in cm^{-1}, and T is the temperature in K (see J. Tennyson et al. 2016 for a detailed description).

To calculate $\Lambda(T)$, we use molecular data from the ExoMol data base (J. Tennyson, C. Hill & S. N. Yurchenko 2013; S. N. Yurchenko & J. Tennyson 2014). We take the CH_4 cooling rate directly from the ExoMol data base, which is based on the older '10to10' line list of S. N. Yurchenko & J. Tennyson (2014). We recomputed the cooling function using the newer 'MM' line list for methane from S. N. Yurchenko et al. (2024), which showed no significant changes. Methane does not have a permanent dipole moment and is therefore an inefficient cooler at Titan temperatures. Conversely, HCN is a strongly dipolar system; we calculate the cooling rate directly using the 'Harris' ExoMol HCN line list (R. J. Barber et al. 2014). This and other cooling functions are in the process of being made available via the new data base of cooling functions hosted on the ExoMol website.

From $\Lambda(T)$, we calculate the total LTE cooling rate for each species as follows:

$$Q_{\rm LTE}(T) = 2\pi\, n\, \Lambda(T), \tag{6}$$

where n is the number density of a given species and the factor 2π accounts for integration over a hemisphere, assuming radiation is emitted in the upward direction only. Since we do not include absorption and re-emission of radiation in our model, we assume that this simplification provides a reasonable estimate of the net LTE cooling rate.

2.2 Chemical network

We updated the chemical network in Kompot with 19 photoreactions (Appendix C, Table C1) and 117 thermal reactions involving only neutrals (Table C2). The wavelength-dependent cross-sections were taken from PHoto Ionization/Dissociation RATES (PHIDRATES) (W. Huebner & J. Mukherjee 2015). Due to the non-availability of photodissociation cross-sections of C_4H_2, C_4H_4, and C_2N_2, we used the UV absorption cross-sections (all

Downloaded from academic.oup.com/mnras/article/553/1/stag1951/8916626 by guest on 10 November 2026

measured below 2400 Å) from the MPI-Mainz UV/VIS Spectral Atlas (H. Keller-Rudek et al. 2013) instead as a proxy and assumed a quantum yield of unity. We consider such an approximation to be reasonable, as photodissociation is expected to dominate over other effects at these wavelengths. Furthermore, any uncertainties introduced by this assumption are expected to have a negligible impact on the model results as this approximation is only applied to the three minor species in Titan's N_2- and CH_4-rich atmosphere.

These newly added chemical reactions are based on the Y. L. Yung et al. (1984) network, with additional reactions from E. Hébrard et al. (2009). We also implemented the reactions involving ammonia (NH_3) from the full S − N − C − H − O network of the open-source photochemical kinetics code VULCAN (S.-M. Tsai et al. 2021). This includes all reactions with NH_2, N_2H, and N_2H_2, as these are important intermediates in NH_3 chemistry. The temperature range and rate coefficients of all newly added reactions were adopted from the KInetics Database for Astrochemistry (KIDA; V. Wakelam et al. 2012). For reactions with multiple rate constants in the literature, we followed KIDA guidelines and selected their recommended values. If no such recommendation was available, we used rate constants from cited works in KIDA, with preference given to values used in models benchmarked against Titan (e.g. E. Hébrard et al. 2009). We calculated the energies associated with each thermal reaction as the difference between the total formation enthalpies of the products and those of the reactants, using enthalpy values from the NIST Chemistry Webbook (P. J. Linstrom & W. G. Mallard 2001, 2025) and the Argonne Active Thermochemical Tables (B. Ruscic & D. Bross 2022; B. Ruscic et al. 2004, 2005). We used the formation enthalpy ($\Delta_f H^\circ$) of each chemical species at the standard temperature of 298.15 K. Furthermore, for some thermal reactions, we adopted updated product channels to reflect our current understanding of Titan's atmospheric composition. As an example, the channel involving the reactants OH and CH_3, which leads to the production of CO in Y. L. Yung et al. (1984), is not included here. Experiments by R. De Avillez Pereira et al. (1997) and D. L. Baulch et al. (2005) suggest alternative channels, none of which produce CO. We include the channels proposed by A.-S. Wong et al. (2002) and the channels from D. L. Baulch et al. (2005) in our chemical network. New calculations are also available for reactions involving a number of other chemical species (B. K. D. Pearce, P. W. Ayers & R. E. Pudritz 2020). However, incorporating these rates would require a broader assessment of the available reaction rates throughout the network to ensure a consistent treatment across all reactions. We therefore retain the reaction rates selected following the methodology described above and defer a systematic evaluation of new reactions and their associated reaction rates to future work.

2.3 Model set-up and input parameters

We perform four model simulations to explore the sensitivity of our results to the choice of eddy diffusion parametrization and to LTE versus non-LTE assumptions in the cooling rate calculations. We benchmark the model results against upper atmospheric observations of Titan. Finally, we use the observation-constrained model to investigate the temporal evolution of Titan's thermal and chemical structure, and Jeans escape rate.

In our model set-up, we adopt a mass of 0.0225 $M_\oplus$, a radius of 0.404 $R_\oplus$, and an orbital distance of 9.45 au to the Sun for Titan.[1] We set the lower boundary of our simulation domain at an altitude of 450 km, which is just below Titan's mesopause[2], thus spanning the entire thermosphere from the mesopause to the exobase. The choice of lower boundary also avoids Titan's dense haze layers, thus minimizing the influence of haze microphysics and radiative effects that are currently not included in our model. The zenith angle was set to an arbitrary angle of 20° as the zenith angle has a negligible effect on the simulated atmospheric profiles. A reference homopause, which separates the well-mixed atmosphere from the stratified atmosphere, was initialized at an altitude of 875 km. The temperature and the number density, held constant at the lower boundary of the simulation domain, were set to 180 K and 4.0×10^{14} cm^{-3}, respectively. These values were adopted to be consistent with observational data (M. Fulchignoni et al. 2005; E. Lellouch et al. 2019; V. Vuitton et al. 2019; A. E. Thelen et al. 2022). During the simulation, however, the atmospheric structure and the homopause are evolved self-consistently until a steady state is reached.

We set the chemistry at the lower boundary of our simulation with a gas mixture composed of N_2, CH_4, CO, and Ar. At 450 km (lower boundary of our simulation grid), Titan's atmospheric CH_4 abundance is constrained by observational data, but no corresponding measurements are known for N_2. Hence, we set the CH_4 mixing ratio (χ_{CH_4}) to 0.02 (D. E. Shemansky et al. 2005; L. Maltagliati et al. 2015). We also initialize a χ_{CO} of 5.0×10^{-5} (J. Serigano et al. 2016). Recent Titan observations with *JWST* show that the CO abundance remains constant throughout the mesosphere and lower thermosphere with an abundance of 55 ± 5 ppm (C. A. Nixon et al. 2025). CO production in Titan is attributed to the influx of O and OH from an external source, as described by S. M. Hörst et al. (2008). While our chemical scheme includes chemical reactions involving O, OH, and CO, our model currently does not account for any external influx of material at the top. Hence, we set the CO abundance at the base of the simulation to the observed values, rather than modelling its production self-consistently. We introduce 50 ppm of Ar at the lower boundary of our simulation as a tracer of vertical transport in our atmospheric model, and to compare against Cassini–Huygens measurements. Although the radiogenic ^{40}Ar is observed in Titan's thermosphere (see V. Vuitton et al. 2024, and references therein), and is commonly used as a tracer, we use bulk argon in our model. Given that ^{40}Ar is the most abundant isotope of argon, and it does not participate in Titan's N_2–CH_4 chemistry, we do not introduce isotopic separation. We adjust the N_2 mixing ratio (χ_{N_2}) to 0.9799 to ensure that the sum of the four mixing ratios is equal to one. The choice of N_2 abundance is in agreement with the ≥0.95 reported in the literature (V. Vuitton et al. 2024).

The primary external energy source in our thermal calculation is the present day solar XUV spectrum, which we take from M. W. Claire et al. (2012). The IR spectrum used here is a simple blackbody with an effective temperature equal to that of the Sun. Joule heating is not expected to have a dominant effect on Titan's thermal profile (D. Snowden & R. V. Yelle 2014), and is hence not

[1] https://www.esa.int/Science_Exploration/Space_Science/Cassini-Huygens/Facts_about_Titan

[2] Titan's reported mesopause altitude varies with instrument and season. We use the definition used in V. Vuitton et al. (2024) and C. A. Nixon et al. (2025).

Downloaded from academic.oup.com/mnras/article/553/1/stag1951/8916626 by guest on 10 November 2026

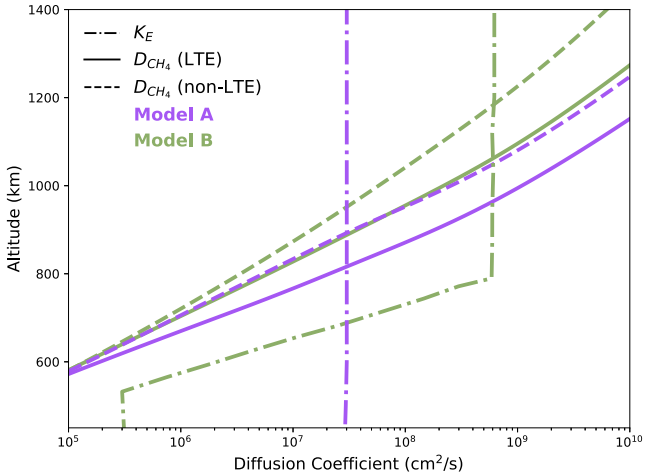


Figure 1. Eddy and molecular diffusion coefficients applied in this work. The dash–dotted lines represent the two K_E profiles used in this work, V. Vuitton et al. (2019; violet) and V. A. Krasnopolsky (2014; green). The solid lines mark the molecular diffusion coefficient of CH_4 calculated for Models A and B, where LTE CH_4 cooling is used in the energy balance equation. The molecular diffusion profiles for the corresponding non-LTE models are shown as dashed lines.

included in our simulations. As for the radiative cooling sources, we consider HCN and CH_4 as they are the dominant emitting molecules in Titan's upper atmosphere. The diffusive flux of particles and conductive flux of energy in our model are controlled by the eddy and the molecular diffusion coefficients. We calculate the molecular diffusion coefficient ($D_{\rm mol}$) self-consistently, but the eddy diffusion coefficient ($K_{\rm E}$) is a free parameter.

Titan's eddy diffusion profile is constrained in the literature by finding a best-fitting model to the chemical abundance profile of nitriles, hydrocarbons, and noble gases observed in Titan's atmosphere, with observations ranging from the stratosphere to the thermosphere. Since $K_{\rm E}$ is not a well-constrained parameter, we tested our simulations against two different eddy diffusion profiles (Models A and B), as shown in Fig. 1. The eddy profile adopted in Model A, while constant in the pressure ranges considered in this work, is based on the asymptotic function fitted by V. Vuitton et al. (2019) to Cassini–Huygens data. The model of V. Vuitton et al. (2019) is one of the most comprehensive photochemical models post Cassini–Huygens, and its adopted eddy diffusion profile is broadly consistent with previous studies (R. Moreno et al. 2012; J. C. Loison et al. 2015). We therefore adopt this $K_{\rm E}$ profile as our baseline case. The eddy diffusion profile of Model B was taken from V. A. Krasnopolsky (2014), which uses a three point profile, with $K_{\rm E}$ on average an order of a magnitude larger than the profile used in Model A, as shown in Fig. 1. The divergence of Model B from Model A can be attributed to the choice in the number of parameters and observational data points used to constrain $K_{\rm E}$, with Model B representing an extreme end of the currently available eddy diffusion estimates for Titan's upper atmosphere. Together, Models A and B are intended to capture the range of uncertainty in the currently available estimates of eddy diffusion coefficients in Titan's upper atmosphere.

Fig. 1 also shows the molecular diffusion profiles of CH_4 ($D_{\rm CH_4}$) calculated within each model. The $D_{\rm CH_4}$ (cm^2 s^{-1}) was calculated using the relation

$$D_{\rm CH_4} = \frac{\alpha_{\rm CH_4} \times 10^{17} T^{S_{\rm CH_4}}}{N}, \quad (7)$$

where T and N represent the temperature and the total number density of the gas. The two coefficients, $\alpha_{\rm CH_4}$ and $S_{\rm CH_4}$, were taken from tabulated values for an N_2-rich atmosphere in P. M. Banks & G. Kockarts (1973). As shown in Fig. 1, the molecular diffusion profile intersects with the eddy diffusion profile at a different altitude in each model. This intersection marks the homopause, which is at an altitude of 800–1050 km for the two LTE models. The homopause for Model A (non-LTE) lies at around 900 km, where as the homopause for Model B (non-LTE) can be found at approximately 1200 km. The precise location of the homopause in a steady-state Kompot simulation is sensitive to the eddy diffusion coefficient, as it affects the density profile, and thus the molecular diffusion coefficient.

3 RESULTS AND DISCUSSION

3.1 Thermal structure

The simulated temperature profiles of our four models are shown in Fig. 2, where the left panel shows a comparison against observational data and the right panel shows a comparison against several existing upper atmospheric models. While the two LTE models exhibit a similar shape for the thermal profile, the absolute temperature values depend heavily on the choice of $K_{\rm E}$ in the model. The temperature structure of the non-LTE Model A is similar to the LTE model B. When compared against the LTE Model A, however, the non-LTE Model A is around 40 K hotter at the lower thermosphere, around 20 K cooler at the middle thermosphere near the homopause, and a few Kelvin hotter at the upper thermosphere. The non-LTE Model B is consistently hotter than the other three models throughout the thermosphere. It also exhibits an almost isothermal behaviour, with a 20 K increase in temperature at the upper thermosphere near the exobase.

In the left panel of Fig. 2, we compare our model results against the temperature profiles derived from data taken by the HASI (M. Fulchignoni et al. 2005), the UVIS (T. T. Koskinen et al. 2011), and the INMS (D. Snowden et al. 2013) instruments aboard Cassini–Huygens, and ALMA (E. Lellouch et al. 2019; A. E. Thelen et al. 2022). Titan's observationally derived temperature profiles show discrepancy across instruments due to instrumental sensitivity, spatial coverage, and seasonal and diurnal variations in Titan (C. A. Nixon et al. 2025). The HASI temperature profile is inferred from *in situ* density measurements and shows the hottest temperatures throughout the thermosphere. T. T. Koskinen et al. (2011) estimated the temperature from CH_4 number densities derived by the Ultaviolet Imaging Spectrograph (UVIS) during two Cassini flybys (T41 and T53). The temperatures from T41 are in good agreement with the measurements of the HASI instrument (not shown here to avoid overcrowding the figure). However, the temperature derived from the T53 fly-by exhibits at least 20 K higher temperature at mid-to-upper thermosphere but much lower temperatures at the mid-to-low thermosphere. Using N_2 densities measured by the INMS instrument, D. Snowden et al. (2013) also estimated Titan's thermospheric temperature structure, which is at least 20 K cooler than other known measurements. The average profile from 32 Cassini passes (square markers), along with the upper and lower bounds (triangular markers) on the uncertainties associated with the derived temperature profiles of

Downloaded from academic.oup.com/mnras/article/553/1/stag1951/8916626 by guest on 10 November 2026

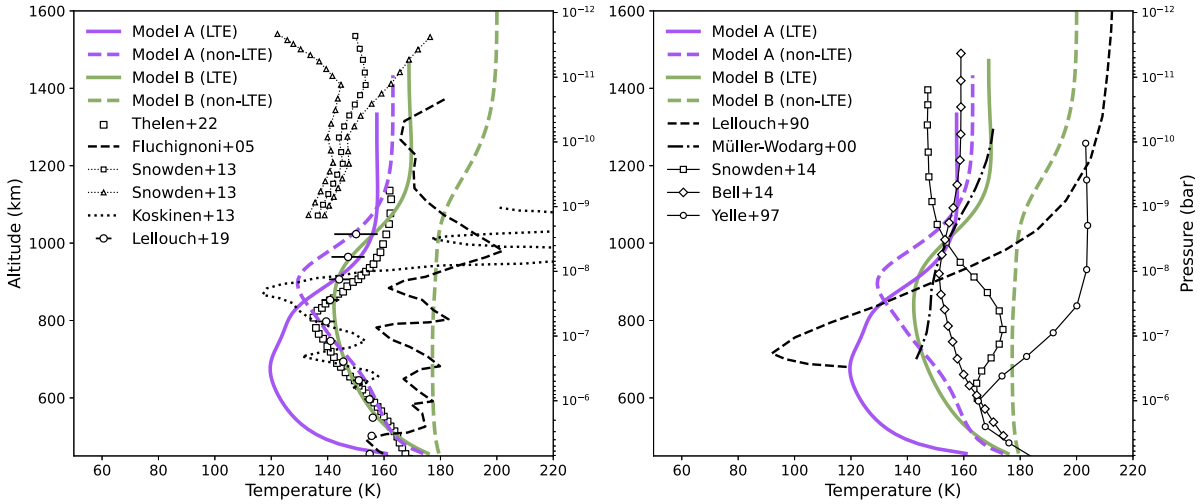


Figure 2. Thermal structure of our four atmospheric models (same colour scheme as in Fig. 1). The temperature in K is shown on the *x*-axis, the altitude in km is shown on the left *y*-axis, and the pressure in bar is shown on the right *y*-axis. Left panel: Temperatures derived from ALMA are marked by squares and circles (A. E. Thelen et al. 2022 and E. Lellouch et al. 2019), from HASI are shown by the dashed line (M. Fulchignoni et al. 2005), and from UVIS are shown by the dotted line (T. T. Koskinen et al. 2011). Globally averaged temperatures from INMS data are shown by the square markers with dotted lines (D. Snowden et al. 2013). The uncertainties associated with the temperature profiles used to calculate the average profile of D. Snowden et al. (2013) are shown by the triangles with dashed lines. Right panel: Temperature profiles from thermospheric models in the literature are shown by the black lines. The solar minimum model of E. Lellouch et al. (2019) is shown by the dashed line, the R. V. Yelle et al. (1997) Titan engineering model is marked by the circles with the solid line, the I. C. F. Müller-Wodarg et al. (2000) model is shown by the dashed and dotted line, the D. Snowden & R. V. Yelle (2014) model is shown by the square markers with the solid line, and the J. M. Bell et al. (2014) model is shown by the diamonds with the solid line.

D. Snowden et al. (2013), is shown in Fig. 2. The temperature profiles retrieved from ALMA HCN and CO observations span multiple epochs, and the best-fitting temperature profiles from E. Lellouch et al. (2019) and A. E. Thelen et al. (2024, 2015 epoch) are shown here, which fall in between the temperature profiles derived using the different Cassini–Huygens instruments.

Depending on the model, our results show varying levels of agreement with the observationally derived temperature profiles. At the mid-to-lower thermosphere (below 800 km), Model A (LTE) is cooler than all observations. However, Model B exhibits strong agreement with the ALMA and the UVIS data. The discrepancy between the LTE Model A simulations and the observations could be due to the missing aerosol heating in our models, which can increase the temperature by approximately 20 K near the bottom of our simulation domain (P. Lavvas et al. 2009). However, as shown by Model A (non-LTE), assumption of non-LTE CH_4 cooling increases the temperature at the lower thermosphere, exhibiting excellent agreement with ALMA observations. At similar altitudes, Model B (non-LTE) is hotter than all other models, but in a better agreement with HASI measurements. At the mid-to-upper thermosphere (above 800 km), the simulated temperature of all models lie within the observed variability. While all four models exhibit some level of agreement with one or multiple sets of observations, Model A (non-LTE) and LTE Model B show a better agreement with the observations, in particular with ALMA.

For completeness, we also compare our results against existing upper atmospheric models on the right panel of Fig. 2. The key differences between our models and other works are the treatment of the stellar XUV heating and the radiative cooling. While Kompot performs a full self-consistent calculation of XUV heating, all other models in the literature apply a simplified approach where the stellar radiation-driven heating is approximated by a parametric heating efficiency factor. The efficiency factor is a free parameter that determines the fraction of the incoming stellar radiation that is converted to heat in the atmosphere. Additionally, the stellar radiation in the X-rays is ignored in the literature models, and only the EUV radiation is considered. The models also differ in terms of the radiative cooling treatment, where they do not always include the same set of molecules in the radiative loss calculation.

The literature temperature profiles that deviate the most from our results are, Titan's engineering model developed by R. V. Yelle et al. (1997) and the model described in E. Lellouch et al. (1990). We show the average temperature profile from R. V. Yelle et al. (1997) and the solar minimum case from E. Lellouch et al. (1990) in the right panel of Fig. 2. Solar EUV heating is incorporated via a heating efficiency factor in both studies. In the 1D atmospheric model of E. Lellouch et al. (1990), the heating efficiency is parametrized by assuming a linear relationship between the efficiency factor and wavelength. The R. V. Yelle et al. (1997) model is an empirical model based on the thermospheric model of R. V. Yelle (1991) where the EUV heating is treated in a similar manner as E. Lellouch et al. (1990). These two models also differ in the treatment of radiative cooling. The E. Lellouch et al. (1990) model incorporates radiative cooling due to CH_4 and C_2H_2, where the calculation is carried out per molecule with a dilution factor to account for non-LTE effects in the upper atmosphere. The R. V. Yelle (1991) calculations include non-LTE radiative cooling of CH_4, C_2H_2, and C_2H_6 under the two-level approximation, and LTE radiative cooling due to HCN. In addition to the treatment of XUV heating and radiative cooling, differences in the input boundary conditions, since these two models were developed before the launch of Cassini–Huygens, could also explain some

Downloaded from academic.oup.com/mnras/article/553/1/stag1951/8916626 by guest on 10 November 2026

of the observed discrepancy between our results and these two models in the literature.

The thermospheric temperatures in our suite of models are in a relatively good agreement with the models of I. C. F. Müller-Wodarg et al. (2000), D. Snowden & R. V. Yelle (2014), and J. M. Bell et al. (2014). However, the temperature structures of these three models deviate from our results at the mid-to-lower thermosphere. This deviation could be primarily attributed to the differences in the complexity of the physical processes included in the various models. All three models treat the stellar EUV heating via an efficiency factor. The simulations of I. C. F. Müller-Wodarg et al. (2000) account for radiative cooling by HCN, but unlike our model, they do not include any CH_4 cooling. The D. Snowden & R. V. Yelle (2014) model, which is based on the R. V. Yelle (1991) model, includes aerosol heating and an additional efficiency term to account for magnetic particle heating. Considering Titan's location within Saturn's magnetosphere, non-thermal heating is considered to be another key heating process in Titan's atmosphere, a process that we do not account for in our model. The thermal profile of D. Snowden & R. V. Yelle (2014) is much hotter (up to 30 K) at mid-to-low thermosphere, which could be attributed to the inclusion of aerosol heating in their model, which is not included in our simulations. Our model B (non-LTE) is a few Kelvin hotter than the D. Snowden & R. V. Yelle (2014) model, but enhanced vertical transport rather than the cooling or the heating rate is responsible for these temperatures. This is supported by the lower temperature in Model A (non-LTE) which employs the same non-LTE cooling as Model B (non-LTE), but differs in terms of the adopted K_E profile. The J. M. Bell et al. (2014) model includes HCN cooling and a fixed magnetic heating term in their thermal calculations. The authors also simulated three different scenarios by varying the diffusion coefficient and an imposed CH_4 escape rate. Out of model simulations described in J. M. Bell et al. (2014), the model with the lowest imposed CH_4 escape rate and higher homopause altitude most closely approximates the observed mixing ratios of CH_4 and HCN. Hence, we only show this model in Fig. 2, which qualitatively agrees with our temperature structure.

As shown in Fig. 2, simulating the thermal structure throughout Titan's upper atmosphere using numerical models is a challenging task. This difficulty is compounded by variability between data taken by different instruments at different phases of Titan's seasonal and diurnal cycles. The data were also collected during the different phases of the solar activity cycle, resulting in variations of the received stellar XUV flux. Our self-consistent treatment of the heating and the cooling terms yields thermospheric temperatures that are well within the range of observed variability, and captures the average temperature structure of Titan's themosphere. The comparable agreement achieved by models incorporating either enhanced eddy diffusion (Model B) or non-LTE radiative cooling (non-LTE Model A) highlights a degeneracy between these mechanisms when considering the thermal structure alone. A detailed discussion on the different heating and cooling terms that shape the temperature structure in our models can be found in Appendix A.

3.2 Chemical composition

3.2.1 Dominant species: N_2 and CH_4

The simulated number densities of the two most abundant atmospheric species, N_2 and CH_4, are compared against observations

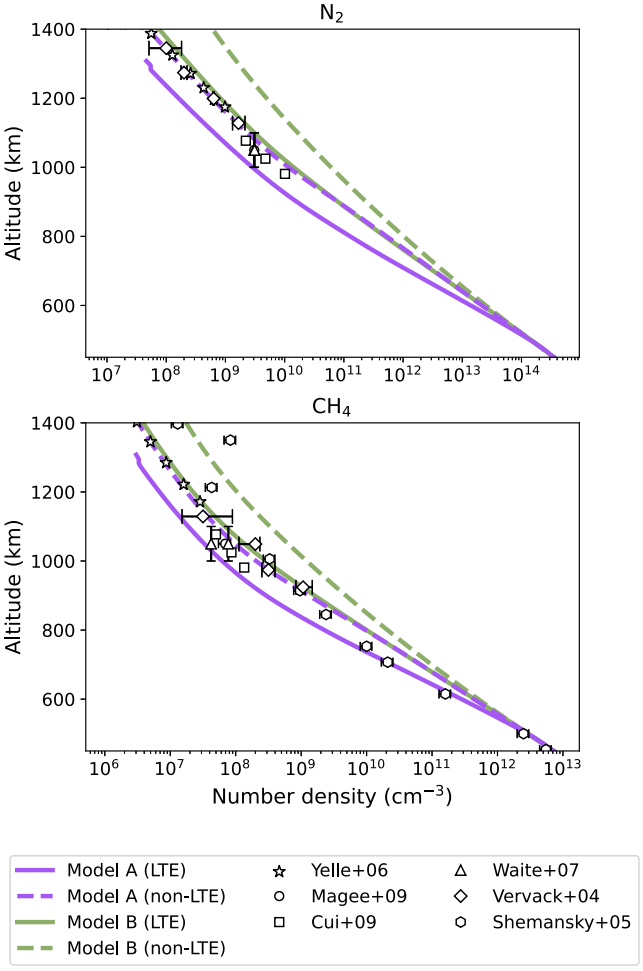


Figure 3. Number densities (cm^{-3}) of N_2 and CH_4 as a function of altitude (km). The colours remain the same as in Fig. 1. The markers represent data taken by Cassini–Huygens and Voyager I.

in Fig. 3. The number density profiles vary within an order of magnitude between the two LTE models, with both N_2 and CH_4 densities increasing with the eddy diffusion coefficient in our models. The non-LTE Model A overlaps the LTE models, but Model B (non-LTE) shows consistently higher densities at the middle and the upper thermosphere. This increase in density from the non-LTE Model A to B correlates with the increase in K_E.

As shown in Fig. 3, Titan's N_2 density measurements are confined to the upper thermosphere (also see fig. 2 in V. Vuitton et al. 2024), and are derived from data taken by Voyager I and Cassini–Huygens' INMS instrument. The number densities shown here were obtained from three separate analyses of INMS data (J. H. Waite et al. 2007; J. Cui et al. 2009; B. A. Magee et al. 2009). To maintain clarity, only the tabulated data from B. A. Magee et al. (2009) are shown. These measurements are marked by the data points at 1000 km and they are in strong agreement with the two LTE models and Model A (non-LTE). INMS data were also analysed by R. V. Yelle et al. (2006), where the authors derived the number densities from both the inward and outward trajectories of Cassini–Huygens. Only the outbound leg is shown here for comparison against our model, which is in excellent agreement with Model A (non-LTE) and the LTE Model B, and within an order of magnitude with LTE Model A. Additionally, we compare

Downloaded from academic.oup.com/mnras/article/553/1/stag1951/8916626 by guest on 10 November 2026

our results against the N_2 values derived by R. J. Vervack, B. R. Sandel & D. F. Strobel (2004) from Voyager I observations, where our model results show the same trend as with the R. V. Yelle et al. (2006) results.

The observationally derived CH_4 number densities are taken from Voyager I, and Cassini–Huygens' INMS and UVIS instruments, leading to a full data coverage of our simulation domain, as shown in Fig. 3. Closer to 1000 km, our model results (two LTE models and the non-LTE Model A) fall well within the variability and any uncertainty associated with the INMS measurements analysed by J. Cui et al. (2009), B. A. Magee et al. (2009), and J. H. Waite et al. (2007). The densities derived by R. V. Yelle et al. (2006) from INMS data, however, are slightly higher at the upper thermosphere which are in excellent agreement with Model A (non-LTE) and Model B, and within an order of magnitude with LTE Model A. The CH_4 densities derived from Voyager I (R. J. Vervack et al. 2004) fall at the middle of our cluster of four models. The CH_4 densities derived from the UVIS data analysis of D. E. Shemansky et al. (2005) are in strong agreement with our LTE models throughout the thermosphere, except at the very top near the exobase. When comparing the non-LTE models, Model A shows a better agreement with this data set at the lower thermosphere, but Model B is in a better agreement with D. E. Shemansky et al. (2005) at the upper thermosphere. Given that the CH_4 number densities derived by D. E. Shemansky et al. (2005) at these altitudes also deviate from the densities derived from INMS data, it could be attributed to the UVIS's poor sensitivity at the upper thermosphere (T. T. Koskinen et al. 2011). New analysis of UVIS data by R. V. Yelle, T. Koskinen & M. Palmer (2021) does not show these very high densities near the exobase. Hence, we consider our model results, except Model B (non-LTE), to be in good agreement with observed CH_4 densities throughout the thermosphere, with Model A (non-LTE) and LTE Model B exhibiting the strongest agreement with the data.

3.2.2 *Minor species*

Figs 4 and 5 show the mixing ratios of a limited selection of six minor species present in Titan's atmosphere, CH_3, C_2H_2, C_2H_4, C_4H_2, HCN, and HC_3N. We selected these species because they were identified in Titan's atmosphere by multiple Cassini–Huygens visits. The methyl radical (CH_3) is also included as it was recently discovered in Titan's atmosphere using *JWST*'s MIRI instrument (C. A. Nixon et al. 2025), although no mixing ratio has been reported so far. The observational data shown here were obtained from Cassini–Huygens' INMS (J. H. Waite et al. 2004; J. Cui et al. 2009; B. A. Magee et al. 2009) and UVIS (T. T. Koskinen et al. 2011) instruments.

In our models, the mixing ratio profiles of these minor species are primarily sensitive to the choice of eddy diffusion. Depending on the species, the choice of CH_4 cooling function has a minor impact. The only exception is CH_3 whose abundance profile does not show any strong correlation with the choice of K_E or CH_4 cooling function. For the other five species with Cassini–Huygens data, agreement between instruments also vary from species to species. Amongst the four models, the LTE model A exhibits a similar trend as the C_2H_2 abundance derived from UVIS data. The two non-LTE models and the LTE Model B are in a better agreement with the INMS derived C_2H_2 abundances. The observed C_2H_4 and HCN abundances show the weakest variability between the instruments. The observed C_2H_4 lies in between our choice of

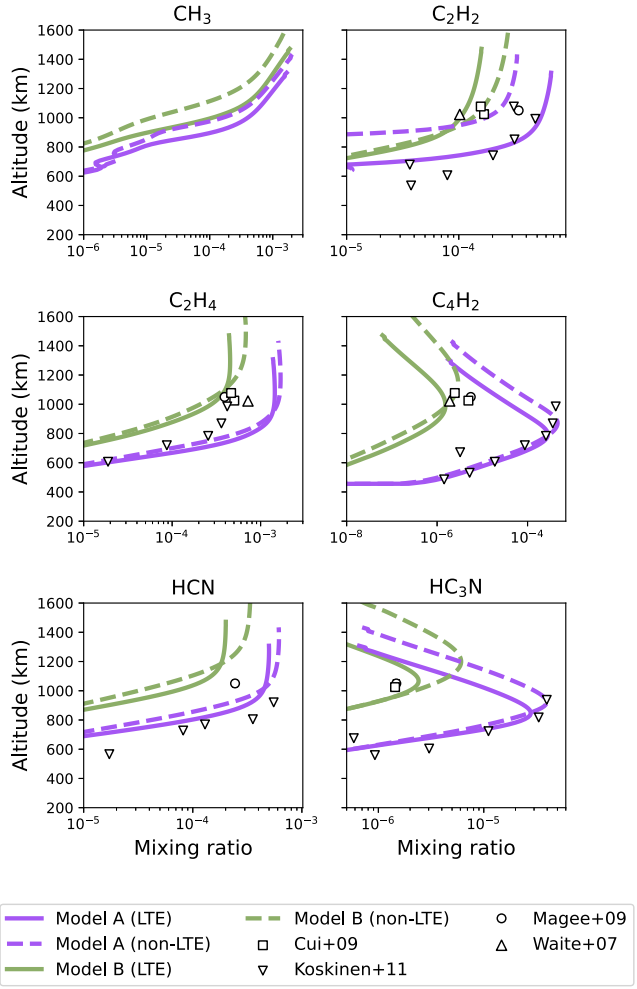


Figure 4. Mixing ratio versus altitude of six minor species, CH_3, C_2H_2, C_2H_4, C_4H_2, HCN, and HC_3N. Our six models have the same colour scheme as in Fig. 1. The open symbols represent the mixing ratios obtained from various observations.

models. However, the HCN abundance is in a better agreement with Models A (LTE and non-LTE). For C_4H_2 and HC_3N, the LTE and the non-LTE model B align with the INMS data but these two models have a significantly lower abundance than the UVIS data. Model A (LTE and non-LTE) are in strong agreement with the UVIS data set. These two models also loosely agree with the INMS data with a slightly higher abundance. When the observed variability in measurements is considered, our ensemble of models captures the average trend in the abundance profile of these minor species.

A comparison of our model results against the photochemical models of Y. L. Yung et al. (1984), E. H. Wilson & S. K. Atreya (2004), P. Lavvas et al. (2008b), V. A. Krasnopolsky (2014), and V. Vuitton et al. (2019) is shown in Fig. 5. The Y. L. Yung et al. (1984) model was developed pre-Cassini–Huygens, so the model assumptions are not as well constrained as the more recent models discussed here. As an example, the chemical kinetics data and reaction pathways have been updated with new laboratory measurements in the last few decades. E. H. Wilson & S. K. Atreya (2004) use the thermal profile from R. V. Yelle et al. (1997, as shown in the right panel of Fig. 2) as an input to calculate the chemical structure. They test their model against a wide range

Downloaded from academic.oup.com/mnras/article/553/1/stag1951/8916626 by guest on 10 November 2026

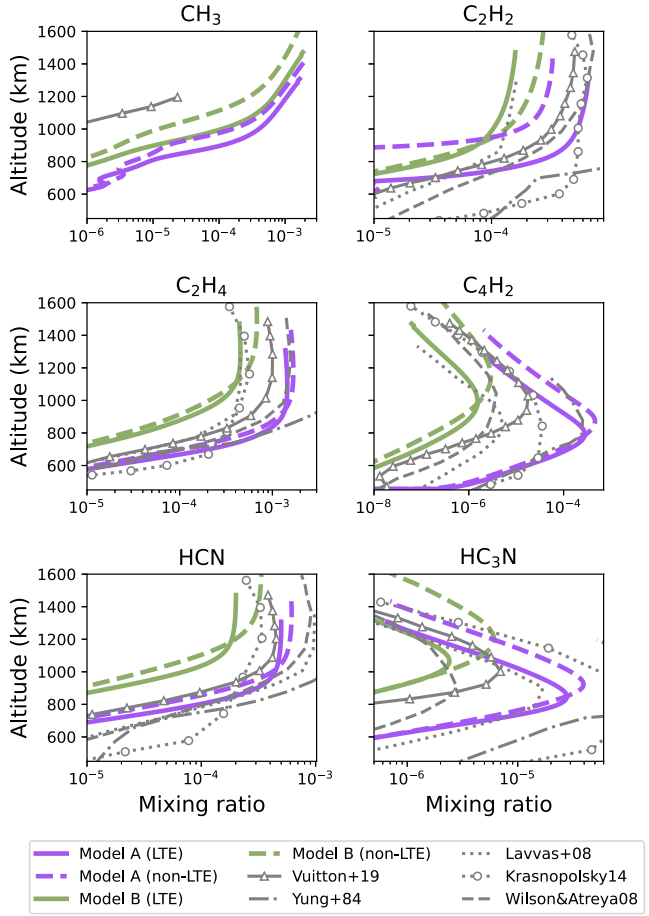


Figure 5. Same as Fig. 4 but model results from the literature are compared instead of observational data. The dashed line represents the model results of E. H. Wilson & S. K. Atreya (2004), the dashed and dotted lines mark the model of Y. L. Yung et al. (1984), the dotted lines are from P. Lavvas et al. (2008b), the dotted lines with open circles show the results from V. A. Krasnopolsky (2014), and the solid line with triangles mark the V. Vuitton et al. (2019) model.

of K_E, and their nominal model is shown here. In addition to photodissociation due to stellar EUV, the model also accounts for cosmic ray deposition. The model of V. A. Krasnopolsky (2014) comprises both neutral and ion chemistry, cosmic ray influx, water delivery at the top of the atmosphere, and magnetospheric electrons and ions. The P. Lavvas et al. (2008b) results shown here are based on their photochemical/microphysics model that accounts for aerosol formation and its impact on gas chemistry. Finally, V. Vuitton et al. (2019) simulates the full atmosphere, extending from the ground to the exobase and includes neutral as well as ion chemistry in their model.

The C_2H_4, C_4H_2, and HCN abundance in the literature models shows a similar structure as our ensemble of models. This suggests that the key reaction pathways connected to these species are captured by all current photochemical models, including ours. However, the profiles of C_2H_2 and HC_3N show varying levels of overlap between our results and other models. While the C_2H_2 and HC_3N profiles from our models broadly agree with the results of V. Vuitton et al. (2019), the abundance of CH_3 is higher in our models. Since our chemical network is not as extensive as some of the networks in the literature, in a future study we will

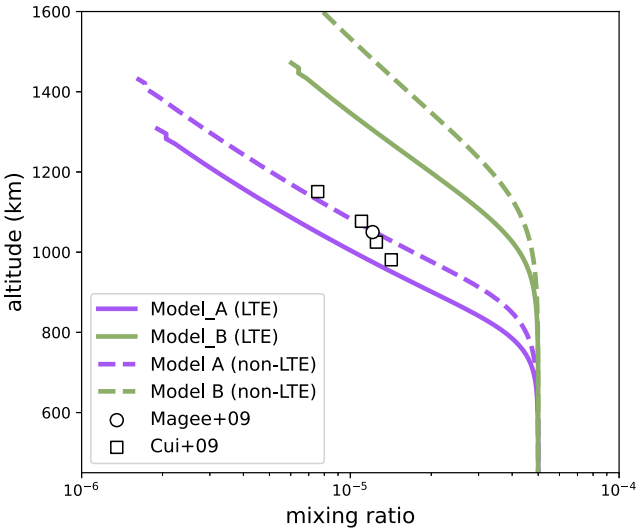


Figure 6. Argon mixing ratio. Same colour scheme as Fig. 1. The markers represent observational data from Cassini–Huygens.

investigate the impact of extended neutral and ion chemistry on the minor species abundance in Titan's upper atmosphere.

3.2.3 Argon abundance

The hydrocarbon and nitrile abundances discussed in the previous section exhibit limited discriminatory power between the models, as different models agree with different subsets of the observations. In contrast, Ar, being chemically inert, is more directly influenced by the atmospheric thermal structure and transport processes. Fig. 6 shows the mixing ratio profile of argon which strongly correlates with the choice of eddy diffusion profile. In general, the argon abundance decreases with an increase in altitude. However, at the upper layers of the thermosphere the abundance is higher for models with stronger vertical mixing. For the same K_E profile, the non-LTE models exhibit higher argon abundance when compared to the LTE models, but the effect is not as strong as the choice of K_E. The Ar abundance measured by the INMS instrument shows good agreement with our weaker K_E models, with the closest match provided by Model A (non-LTE).

3.3 Atmospheric escape

Table 1 lists the top five chemical species by Jeans escape rate in our four models. In Model A (LTE), H, H_2, H^+, H_2^+, and H_3^+ exhibit the largest escape rates where as in Model B (LTE), CH_4 and CH_3 have stronger Jeans escape than H_2^+ and H_3^+. In Model A (non-LTE), the species list changes to H, H_2, H^+, H_2^+, and CH_4, whereas in the case of Model B (non-LTE), N rather than H_2^+ appears in the list of five species with the strongest Jeans escape.

Titan's inferred H escape rate from Cassini–Huygens observations by P. Hedelt et al. (2010) is 2.8×10^3 g s^{-1}. However, D. F. Strobel & J. Cui (2014) estimate an escape rate of 1.7×10^3 g s^{-1}, highlighting the difficulty in constraining Titan's H escape rate. The H_2 escape rate is however, calculated over multiple Cassini–Huygens flybys, with an approximate value of 3.1×10^4 g s^{-1} (I. Müller-Wodarg et al. 2014). The Jeans escape of atomic and molecular hydrogen calculated in our models varies by a factor of a few or an order of magnitude from these observed escape

Downloaded from academic.oup.com/mnras/article/553/1/stag1951/8916626 by guest on 10 November 2026

Table 1. Top five chemical species by Jeans escape. Eight chemical species are shown, as the top five species are not the same in all models. Both escape rate in units of g s^{-1} and flux in units of cm^{-2} s^{-1} (in brackets) are included. Observationally determined escape rates and escape fluxes (in brackets) are also shown, separated from our model results by a horizontal line.

Model	H $\times 10^5$	H_2 $\times 10^4 (\times 10^9)$	H^+ $\times 10^1$	$H_2{}^+$ $\times 10^{-4}$	$H_3{}^+$ $\times 10^{-4}$	CH_4 $\times 10^{-3}$	CH_3 $\times 10^{-4}$	N $\times 10^{-2}$
A (LTE)	0.2	0.8(2.8)	0.3	0.6	0.2			
B (LTE)	0.6	0.4(1.4)	0.2			0.2(9.0)	0.6	
A (non-LTE)	0.3	0.3(1.1)	0.4	2.9		0.1(5.0)		
B (non-LTE)	0.1	1.4(5.1)	0.2			69.3(3.1×10^3)		0.9
P. Hedelt et al. (2010)	0.03							
D. F. Strobel & J. Cui (2014)	0.02	3.1						
R. V. Yelle et al. (2006)		(12±2)						
J. Cui, R. V. Yelle & K. Volk (2008)		(13.7±0.1)						
R. V. Yelle, J. Cui & I. C. F. Müller-Wodarg (2008)						(2.8×10^9)		
J. Cui et al. (2012)						(3.6×10^9)		

rates. To the best of our knowledge, the individual escape rates of hydrogen ions and atomic nitrogen have not yet been measured by any instrument.

By fitting a diffusion model to observed H_2 abundance, R. V. Yelle et al. (2006) determined an H_2 diffusive flux of $5.8 \pm 0.1 \times 10^9$ cm^{-2} s^{-1} at an altitude of 1200 km. The R. V. Yelle et al. (2006) model adopted a K_E of 4×10^9 cm^{-2} s^{-1}, which is almost an order of magnitude higher than our Model B. The authors used their diffusion flux to calculate a diffusion-limited escape flux scaled to the surface (hereafter, in this subsection, scaled to the surface flux is simply referred to as flux), which is equal to $1.2 \pm 0.2 \times 10^{10}$ cm^{-2} s^{-1}. Using a larger sample of Cassini–Huygens' INMS data, J. Cui et al. (2008) also fitted a diffusive flux model to the observed H_2 distribution and estimated a flux of $1.37 \pm 0.01 \times 10^{10}$ cm^{-2} s^{-1}. The eddy diffusion coefficient used in J. Cui et al. (2008) is based on R. V. Yelle et al. (2008). The diffusive flux in both studies is almost an order of magnitude higher than their estimated Jeans escape flux. J. Cui et al. (2008) state that the disagreement between Titan's Jeans escape and diffusion-limited escape of H_2 can be addressed by adopting a non-Maxwellian velocity distribution for the gas at the exobase.

Instead of fitting our models to observations, we self-consistently solve for the temperature and chemical structure of Titan's upper atmosphere and calculate the thermal Jeans escape rate, which we then convert to escape flux for comparison against the diffusion-limited escape flux in the literature. The calculation of Jeans escape reported in our models is based on S. J. Bauer & H. Lammer (2004), which considers a Maxwellian velocity distribution. As shown in Table 1, the Jeans escape flux of our models differs from the escape flux reported in R. V. Yelle et al. (2006) and J. Cui et al. (2008) by anywhere from a factor of a few to an order of magnitude, depending on the K_E assumption in our model. This discrepancy in escape flux is within the expected uncertainties arising from differences in chemical networks, diffusion, and energy balance. Hence, we argue that a Maxwellian assumption is reasonable in the calculation of Jeans escape of H_2 in Titan.

To further support our argument, we have plotted the H_2 mixing ratio from our models together with Cassini–Huygens INMS-derived H_2 abundances in Fig. 7. The observed values reported by B. A. Magee et al. (2009) and J. Cui et al. (2009) at an altitude of ∼1000 km are higher by a factor of 2–3 when compared against the LTE and the non-LTE Model A, and approximately an order of magnitude when compared against the LTE and the non-LTE Model B. The reported H_2 abundances in R. V. Yelle et al. (2006) are in excellent agreement with Model A (LTE and non-LTE). The R. V. Yelle et al. (2006) results, however, disagree with Model B (LTE and non-LTE) by at least an order of magnitude. In general, our self-consistent models with weaker eddy diffusion coefficients are in better agreement with observations, and no strong preference is seen for either LTE or non-LTE models in such cases.

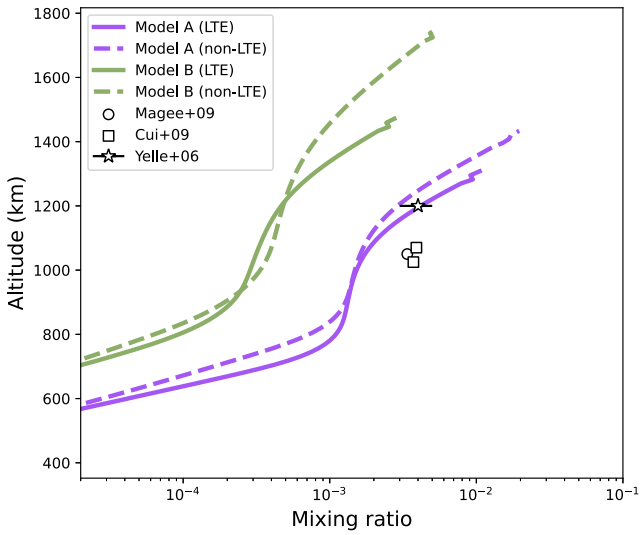


Figure 7. H_2 mixing ratio versus altitude in kilometre. The coloured lines represent the model results that follow the same colour scheme as in Fig. 1. The markers represent H_2 mixing ratios determined from Cassini–Huygens/INMS observations.

In addition to H_2, CH_4 escape is speculated to play an important role in the long-term evolution of Titan's atmospheric chemistry and aerosol properties. However, there is no clear consensus around Titan's CH_4 escape rate. R. V. Yelle et al. (2008) hypothesizes that a diffusive model with strong upward flow can explain high CH_4 abundances, which can be as high as 10 per cent in terms of the total gas near the exobase (Fig. 8), and a CH_4 escape flux of 2.8×10^9 cm^{-2} s^1 best fits this data. A newer study with additional Cassini–Huygens INMS data estimates the escape rate to be approximately 8×10^4 g s^{-1} (J. Cui et al. 2012), which leads to an escape flux of 3.6×10^9 cm^{-2} s^{-1}. The Jeans escape of CH_4 in our models is negligible. We calculated a CH_4 escape

Downloaded from academic.oup.com/mnras/article/553/1/stag1951/8916626 by guest on 10 November 2026

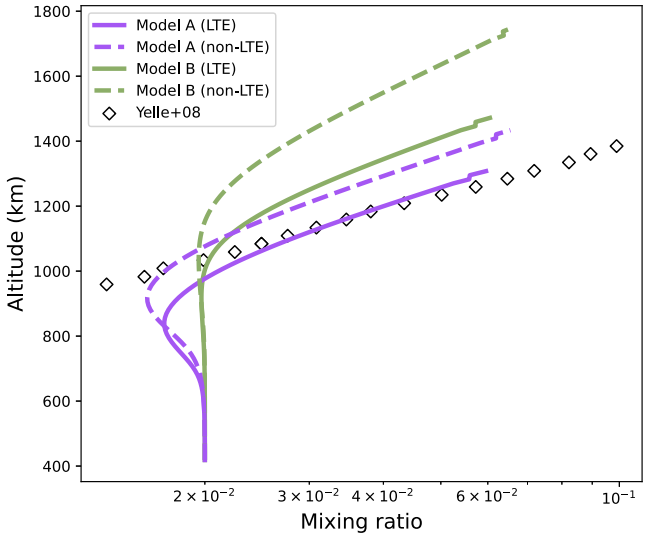


Figure 8. CH_4 mixing ratio versus altitude in kilometre, same colour scheme as Fig. 1. The Cassini–INMS data analysed by R. V. Yelle et al. (2008) are shown by the diamond markers.

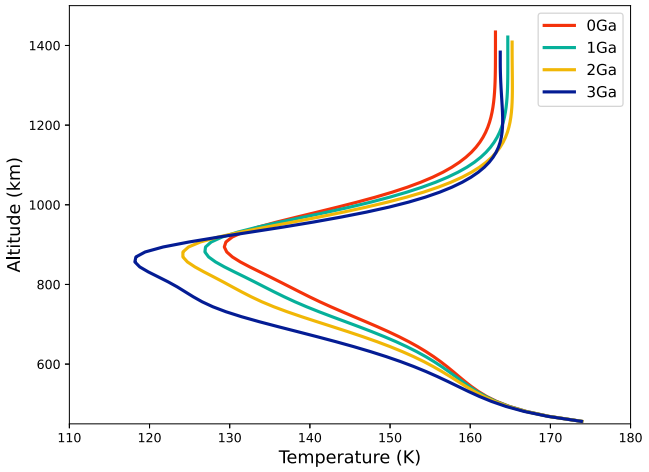


Figure 9. Titan's upper atmospheric temperature over time. The orange line represents present-day Titan, specifically Model A (non-LTE). The green, yellow, and dark blue lines represent 1, 2, and 3 Ga in the past, respectively.

flux of 9.0, 5.0, and 3.1 $\times$ 10^3 cm^{-2} s^{-1} for Model B (LTE), Model A (non-LTE), and Model B (non-LTE), respectively, which are orders of magnitude lower than the estimated diffusion-limited escape fluxes.

Despite this large discrepancy in escape fluxes, the CH_4 abundances in our models are in good agreement with CH_4 abundances derived from Cassini–Huygens data. Fig. 8 shows that the CH_4 abundances derived from Model A (LTE and non-LTE) show excellent agreement with the observed high abundance of CH_4, despite exhibiting negligible Jeans escape of CH_4. Model A (non-LTE) is at most a factor of two lower in abundance when compared to the observed data. At an altitude of 1000 km, the non-LTE Model A has marginally better agreement over the LTE Model A. The CH_4 mixing ratio profiles derived from the non-LTE Model B, our model with the largest CH_4 escape flux, is lower than the observed abundances by an order of magnitude or more. The LTE Model B exhibits slightly lower abundances when compared against the non-LTE Model A. This shows that our self-consistent models reproduce observed abundances of CH_4 without invoking strong eddy diffusion. The agreement between the observed and the model abundances in Fig. 8 does not support the theory of strong atmospheric CH_4 escape into space.

3.4 Temporal evolution of Titan's upper atmosphere

Although our models predict negligible thermal escape of CH_4 under present-day Titan conditions, we investigate whether CH_4 could have been lost more efficiently through thermal Jeans escape earlier in Titan's history. Since the abundance of atmospheric CH_4 over Titan's history is not well known, we retain the present-day atmospheric composition in all simulations. It has been suggested that the atmospheric CH_4 reservoir on present-day Titan is relatively young, with an age of $\leq$1 Ga (G. Tobie et al. 2006). Therefore, CH_4 may not have been present in significant amounts 2–3 Ga ago. Nevertheless, we extend our simulations to 3 Ga as a hypothetical exercise to investigate how Titan's upper atmosphere would have responded to the enhanced solar XUV flux if Titan's present-day atmosphere had existed at those epochs.

We explore Titan's atmospheric evolution using the same set of assumptions as used in Model A (non-LTE), as it offers the best observationally constrained representation of Titan's upper atmosphere. We use solar XUV spectra in time generated by the model of M. W. Claire et al. (2012). Fig. 9 shows the temporal evolution of Titan's upper atmospheric temperature structure, which does not show any significant increase in the upper thermosphere, but instead exhibits a relatively cooler temperature in the middle thermosphere for early Titan. The increase in solar XUV flux between now and 3 Ga ago leads to increased XUV absorption at the upper atmosphere. Although the solar XUV flux is stronger in the past, much of the XUV energy is absorbed in the upper thermosphere, limiting the increase in XUV heating at lower altitudes (see Appendix B for further details). In addition, an increase in the XUV flux also enhances the production of HCN, via the photolysis of CH_4 and N_2. Fig. 10 shows the temporal evolution of HCN and CH_4 abundance in Titan's upper atmosphere. The enhanced HCN abundance increases the HCN number density throughout the upper atmosphere, strengthening HCN radiative cooling. Since the enhanced HCN cooling is not fully compensated by local XUV heating, it results in lower temperatures in the middle thermosphere.

The Jeans escape from our three additional steady-state models exhibits a similar trend as the 0 Ga model (non-LTE Model A). Atomic hydrogen (H) exhibits the strongest Jeans escape in all three models. Jeans escape of CH_4 is identical between 0 and 1 Ga. However, at 2 and 3 Ga, Jeans escape of H, H_2, and H ions dominates over CH_4 loss. This is not surprising, as the abundance of CH_4 decreases with increase in time from the present.

4 CONCLUSIONS

We updated the 1D atmospheric code Kompot, and benchmarked our model against observations of Titan's upper atmospheric thermal and chemical structure. We further assessed the sensitivity of the model to the choice of eddy diffusion coefficient profile and to the treatment of CH_4 radiative cooling under LTE and non-LTE assumptions.

Our simulated upper atmospheric temperature structures fall within the range of temperature profiles derived from observa-

Downloaded from academic.oup.com/mnras/article/553/1/stag1951/8916626 by guest on 10 November 2026

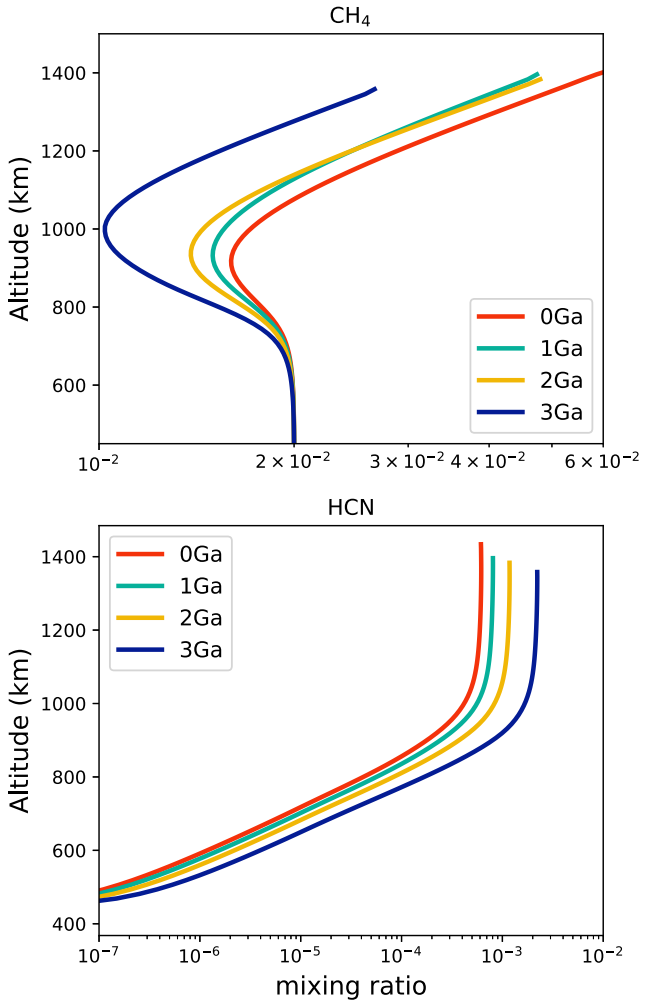


Figure 10. Mixing ratio of CH_4 (top panel) and HCN (bottom panel) over time. Same colour scheme as in Fig. 9.

tions. This suggests that energy balance between HCN and CH_4 radiative cooling, XUV and chemical heating, and conduction reproduces Titan's thermospheric temperature profile within observed variations. Additional physics not considered in this work, such as aerosol heating, could modify the temperature structure locally, but the overall temperature structure would still be governed by the key mechanisms included in our model. The non-LTE Model A and the LTE Model B produce temperature profiles that both fall within the central portion of the observed variability of Titan's upper atmospheric temperature measurements. Although the two models differ in their assumptions regarding eddy diffusion and CH_4 radiative cooling, they achieve comparable agreement with the observations. This suggests that the thermal structure alone does not uniquely constrain these model parameters, as different combinations of eddy diffusion and radiative cooling treatment can reproduce similar temperature profiles.

The chemical abundance profiles from our models show varying levels of agreement with observed abundances. The model N_2 and CH_4 number density profiles exhibit a similar trend as the temperature structure, where Models A (non-LTE) and Model B (LTE) show the strongest agreement with observational data. However, for the minor species, the level of agreement between our models and observations is species dependent. Furthermore, depending on the observational data set, either Models B (LTE and non-LTE) or Models A (LTE and non-LTE) are in a better agreement with the data. Comparison of our model Ar abundance profile show that both LTE and non-LTE Model A are broadly consistent with the observations, but Model A (non-LTE) provide a better match with observations. Since Ar is a noble gas, its abundance profile is governed primarily by vertical transport, providing a better constraint for the eddy diffusion profile. Thus, when combined with the temperature structure results, the non-LTE Model A, with weaker eddy diffusion, provides the most consistent description of Titan's upper atmospheric temperature structure and chemistry.

Our results highlight the importance of self-consistently modelling the coupled thermal and chemical structure of planetary upper atmospheres. This is particularly relevant for exoplanet atmospheres, where the temperature structure is not known a priori. Different transport and radiative processes can produce similar temperature profiles, while their coupled effects on the chemical composition and temperature can differ substantially. Simultaneously modelling these feedbacks, and combining thermal and chemical constraints, can therefore help break certain degeneracies and constrain the underlying processes in planetary upper atmospheres.

We also calculated the Jeans escape rates at Titan's exobase and identified neutral and ionized hydrogen to have the largest escape fluxes. Nonetheless, our thermal H_2 escape fluxes are weaker than those inferred in the literature under the diffusion-limited regime, where diffusion models are fitted to observationally derived H_2 abundances. While comparing our model H_2 abundances with the observed values, we find that models with weaker eddy diffusion coefficients, both LTE and non-LTE Model A, exhibit better agreement with the data. We hypothesize that the external influx of H_2O from Enceladus, rather than very strong diffusion, could at least partially explain the observed overabundance of H_2 in Titan's upper thermosphere. The Jeans escape of CH_4 is negligible in our models, except in the case of Model B (non-LTE). However, the CH_4 escape flux in Model B (non-LTE) is more than six orders of magnitude lower when compared to diffusion-limited escape flux calculations from Cassini–Huygens observations. Our models show that a relatively high abundance of CH_4, similar to the ones seen in Cassini–Huygens observations, can be achieved without invoking strong diffusion or escape rates. Our results do not support strong CH_4 escape from Titan's atmosphere, even when early Sun's XUV fluxes are considered.

Finally, our model is 1D, whereas Titan's atmosphere is 3D, and the available observations span different seasons, local times, and atmospheric pressure regimes. Future work will therefore require both increasingly comprehensive models and observations that provide more coordinated constraints on the atmospheric thermal and chemical structure. As an example, inclusion of energetic and radiative feedback from haze particles in the model would enhance our predictive capability for the mesospheric thermal and chemical structure. As model complexity increases, coordinated observations that constrain the same atmospheric regions and conditions will be essential for distinguishing between the effects of different atmospheric processes and for ensuring that model complexity remains physically and observationally justified. These considerations are also directly relevant to exoplanet atmospheric modelling, where observational constraints are typically much more limited and Titan provides an impor-

Downloaded from academic.oup.com/mnras/article/553/1/stag1951/8916626 by guest on 10 November 2026

tant Solar-system laboratory for developing and testing such approaches.

ACKNOWLEDGEMENTS

We thank the anonymous referee for their valuable comments which have helped us improve the manuscript. This work was partly supported by the ASAP project APPLE-Kompot, funded by the Austrian Forschungsförderungsgesellschaft (FFG) through BMIMI, and the European Research Council (ERC) project EASE, 101123041. Work performed at UCL was supported by the ERC under the European Union's Horizon 2020 research and innovation programme via Advanced Grant 883830. Views and opinions expressed are however those of the author(s) only and do not necessarily reflect those of the European Union or the European Research Council Executive Agency. Neither the European Union nor the granting authority can be held responsible for them.

DATA AVAILABILITY

The observational data used in this work are taken from previously published work. The data related to the chemical network update are provided in the appendix.

REFERENCES

Banks P. M., Kockarts G., 1973, Aeronomy. Academic Press, New York, NY
Barber R. J., Strange J. K., Hill C., Polyansky O. L., Mellau G. C., Yurchenko S. N., Tennyson J., 2014, MNRAS, 437, 1828
Bauer S. J., Lammer H., 2004, Planetary Aeronomy: Atmosphere Environments in Planetary Systems. Springer, Berlin
Baulch D. L. et al., 2005, J. Phys. Chem. Ref. Data, 34, 757
Beatty T. G. et al., 2024, ApJ, 970, L10
Bell J. M. et al., 2010, J. Geophys. Res., 115, E12002
Bell J. M., Hunter Waite J., Westlake J. H., Bougher S. W., Ridley A. J., Perryman R., Mandt K., 2014, J. Geophys. Res.: Space Phys., 119, 4957
Berteloite C., Le Picard S. D., Balucani N., Canosa A., Sims I. R., 2010, Phys. Chem. Chem. Phys., 12, 3666
Claire M. W., Sheets J., Cohen M., Ribas I., Meadows V. S., Catling D. C., 2012, ApJ, 757, 95
Cravens T. E. et al., 2009, Icarus, 199, 174
Cui J., Yelle R. V., Volk K., 2008, J. Geophys. Res., 113, 2007JE003032
Cui J. et al., 2009, Icarus, 200, 581
Cui J., Yelle R. V., Strobel D. F., Müller-Wodarg I. C. F., Snowden D. S., Koskinen T. T., Galand M., 2012, J. Geophys. Res., 117, 2012JE004222
De Avillez Pereira R., Baulch D. L., Pilling M. J., Robertson S. H., Zeng G., 1997, J. Phys. Chem. A, 101, 9681
Dobrijevic M., Loison J., Hickson K., Gronoff G., 2016, Icarus, 268, 313
Douglas K., Blitz M. A., Feng W., Heard D. E., Plane J. M., Slater E., Willacy K., Seakins P. W., 2018, Icarus, 303, 10
Fulchignoni M. et al., 2005, Nature, 438, 785
Gannon K. L., Blitz M. A., Kovács T., Pilling M. J., Seakins P. W., 2010, J. Chem. Phys., 132, 024302
Gronoff G., Lilensten J., Desorgher L., Flückiger E., 2009, A&A, 506, 955
Guilluy G. et al., 2022, A&A, 665, A104
Harada N., Herbst E., 2008, ApJ, 685, 272
Hébrard E. et al., 2009, J. Phys. Chem. A, 113, 11227
Hedelt P., Ito Y., Keller H., Reulke R., Wurz P., Lammer H., Rauer H., Esposito L., 2010, Icarus, 210, 424
Herron J. T., 1999, J. Phys. Chem. Ref. Data, 28, 1453
Hörst S. M., 2017, J. Geophys. Res., 122, 432
Hörst S. M., Vuitton V., Yelle R. V., 2008, J. Geophys. Res., 113, E10006
Huebner W., Mukherjee J., 2015, Planet. Space Sci., 106, 11
Huo R.-P., Zhang X., Huang X.-R., Li J.-L., Sun C.-C., 2011, J. Phys. Chem. A, 115, 3576
Jaziri A. Y., Sohier O., Venot O., Carrasco N., 2025, A&A. 701A, 33
Johnstone C. P., 2020, ApJ, 890, 79
Johnstone C. P., Güdel M., Lammer H., Kislyakova K. G., 2018, A&A, 617, A107
Johnstone C. P., Khodachenko M. L., Lüftinger T., Kislyakova K. G., Lammer H., Güdel M., 2019, A&A, 624, L10
Keller-Rudek H., Moortgat G. K., Sander R., Sörensen R., 2013, Earth Syst. Sci. Data, 5, 365
Klippenstein S. J., Harding L. B., Ruscic B., Sivaramakrishnan R., Srinivasan N. K., Su M.-C., Michael J. V., 2009, J. Phys. Chem. A, 113, 10241
Koskinen T. T., Yelle R. V., Snowden D. S., Lavvas P., Sandel B. R., Capalbo F. J., Benilan Y., West R. A., 2011, Icarus, 216, 507
Krasnopolsky V. A., 2014, Icarus, 236, 83
Lavvas P., Coustenis A., Vardavas I., 2008a, Planet. Space Sci., 56, 27
Lavvas P., Coustenis A., Vardavas I., 2008b, Planet. Space Sci., 56, 67
Lavvas P., Yelle R. V., Vuitton V., 2009, Icarus, 201, 626
Lellouch E., Hunten D. M., Kockarts G., Coustenis A., 1990, Icarus, 83, 308
Lellouch E. et al., 2019, Nat. Astron., 3, 614
Linstrom P. J., Mallard W. G., 2001, J. Chem. Eng. Data, 46, 1059
Linstrom P. J. Mallard W. G., 2025, NIST Chemistry WebBook: NIST Standard Reference Database No. 69. National Institute of Standards and Technology, Gaithersburg, MD
Loison J.-C., Wakelam V., Hickson K. M., 2014, MNRAS, 443, 398
Loison J. C. et al., 2015, Icarus, 247, 218
Madhusudhan N., Sarkar S., Constantinou S., Holmberg M., Piette A. A. A., Moses J. I., 2023, ApJ, 956, L13
Magee B. A., Waite J. H., Mandt K. E., Westlake J., Bell J., Gell D. A., 2009, Planet. Space Sci., 57, 1895
Maltagliati L. et al., 2015, Icarus, 248, 1
Moreno R., Lellouch E., Lara L. M., Feuchtgruber H., Rengel M., Hartogh P., Courtin R., 2012, Icarus, 221, 753
Müller-Wodarg I., Griffith C. A., Lellouch E., Cravens T. E., 2014, Titan: Interior, Surface, Atmosphere, and Space Environment, 1 edn. Cambridge Univ. Press, Cambridge
Müller-Wodarg I. C. F., Yelle R. V., Mendillo M., Young L. A., Aylward A. D., 2000, J. Geophys. Res., 105, 20833
Nixon C. A., 2024, ACS Earth Space Chem., 8, 406
Nixon C. A. et al., 2025, Nat. Astron., 9, 969
Pagsberg P. B., Eriksen J., Christensen H. C., 1979, J. Phys. Chem., 83, 582
Pearce B. K. D., Ayers P. W., Pudritz R. E., 2020, J. Chem. A, 124, 8594
Rezac L., Kutepov A. A., Faure A., Hartogh P., Feofilov A. G., 2013, A&A, 555, A122
Ruscic B. et al. 2004, J. Phys. Chem. A, 108, 9979
Ruscic B. et al. 2005, J. Phys.: Conf. Ser., 16, 561
Ruscic B., Bross D., 2022, Active Thermochemical Tables (ATcT) Thermochemical Values, ver. 1.122v.
Samu V., Varga T., Rahinov I., Cheskis S., Turányi T., 2018, Fuel, 212, 679
Serigano J., Nixon C. A., Cordiner M. A., Irwin P. G. J., Teanby N. A., Charnley S. B., Lindberg J. E., 2016, ApJ, 821, L8
Shemansky D. E., Stewart A. I. F., West R. A., Esposito L. W., Hallett J. T., Liu X., 2005, Science, 308, 978
Snowden D., Yelle R. V., 2014, Icarus, 228, 64
Snowden D., Yelle R. V., Cui J., Wahlund J. E., Edberg N. J. T., Ågren K., 2013, Icarus, 226, 552
Strobel D. F., 1974, Icarus, 21, 466
Strobel D. F., Cui J., 2014, in Müller-Wodarg I., Griffith C. A., Lellouch E., Cravens T. E., eds, Titan, 1st edn. Cambridge Univ. Press, Cambridge, p. 355
Sumathi R., Peyerimhoff S., 1996, Chem. Phys. Lett., 263, 742
Taylor J., 2025, Res. Notes Am. Astron. Soc., 9, 118
Tennyson J., Hill C., Yurchenko S. N., 2013, AIP Conf. Proc. Vol. 1545, Data Structures for ExoMol: Molecular Line Lists for Exoplanet and Other Atmospheres. Am. Inst. Phys., New York, p. 186 10.1063/1.4815853

Downloaded from academic.oup.com/mnras/article/553/1/stag1951/8916626 by guest on 10 November 2026

Tennyson J., Hulme K., Naim O. K., Yurchenko S. N., 2016, J. Phys. B: At. Mol. Opt. Phys., 49, 044002
Thelen A. E., Nixon C. A., Cosentino R. G., Cordiner M. A., Teanby N. A., Newman C. E., Irwin P. G. J., Charnley S. B., 2022, Planet. Sci. J., 3, 146
Thelen A. E. et al., 2024, Planet. Sci. J., 5, 125
Tobie G., Lunine J. I., Sotin C., 2006, Nature, 440, 61
Tomasko M. G. et al., 2005, Nature, 438, 765
Tsai S.-M., Malik M., Kitzmann D., Lyons J. R., Fateev A., Lee E., Heng K., 2021, ApJ, 923, 264
Tsai S.-M. et al., 2023, Nature, 617, 483
Van Looveren G., Güdel M., Boro Saikia S., Kislyakova K., 2024, A&A, 683, A153
Van Looveren G., Boro Saikia S., Herbort O., Schleich S., Güdel M., Johnstone C., Kislyakova K., 2025, A&A, 694, A310
Vervack R. J., Sandel B. R., Strobel D. F., 2004, Icarus, 170, 91
Vuitton V., Yelle R. V., Klippenstein S. J., Hörst S. M., Lavvas P., 2019, Icarus, 324, 120
Vuitton V., Lavvas P., Nixon C., Teanby N., 2024, Titan After Cassini-Huygens. Elsevier
Waite J. H. et al., 2004, Space Sci. Rev., 114, 113
Waite J. H., Crary F. J., Young D. T., Magee B. A., Mandt K., 2007, DPS Meeting, 39, 63.01
Wakelam V. et al., 2012, ApJS, 199, 21
Wilson E. H., Atreya S. K., 2004, J. Geophys. Res., 109, E06002
Wong A.-S., Morgan C. G., Yung Y. L., Owen T., 2002, Icarus, 155, 382
Xue Q. et al., 2025, ApJ, 995, L52
Yelle R. V., 1991, ApJ, 383, 380
Yelle R. V., Strobell D. F., Lellouch E., Gautier D., 1997, in Wilson A, ed., Proc. ESA Conf., Huygens: Science, Payload and Mission. p. 243
Yelle R. V., Borggren N., De La Haye V., Kasprzak W., Niemann H., Müller-Wodarg I., Waite J., 2006, Icarus, 182, 567
Yelle R. V., Cui J., Müller-Wodarg I. C. F., 2008, J. Geophys. Res., 113, E10003
Yelle R. V., Vuitton V., Lavvas P., Klippenstein S. J., Smith M. A., Hörst S. M., Cui J., 2010, Faraday Discuss., 147, 31
Yelle R. V., Koskinen T., Palmer M., 2021, Icarus, 368, 114587
Yung Y. L., Allen M., Pinto J. P., 1984, ApJS, 55, 465
Yurchenko S. N., Tennyson J., 2014, MNRAS, 440, 1649
Yurchenko S. N., Owens A., Kefala K., Tennyson J., 2024, MNRAS, 528, 3719
Zieba S. et al., 2023, Nature, 620, 746

APPENDIX A: HEATING AND COOLING RATES FOR PRESENT-DAY TITAN

Fig. A1 shows the key contributors to the total heating and cooling rate for Model A (non-LTE). The total heating rate is dominated by XUV heating, followed by chemical heating. IR heating is the third dominant heating mechanism, but it is orders of magnitude weaker than XUV and chemical heating. At the lower thermosphere, the total cooling is dominated by radiative cooling by CH_4, but HCN cooling takes over at the middle and upper thermosphere. Near the lower boundary of our simulations, thermal conduction balances the strong radiative cooling rate by CH_4. The energy balance between these heating and cooling profiles, together with conduction, leads to the temperature structure in our four atmospheric models, as shown in Fig. 2.

Figs A2 and A3 show the volumetric energy rates and the energy rates per unit mass for the dominant heating and cooling processes in our models. The volumetric XUV heating (Fig. A2, top left) peaks in the mid-to-lower thermosphere, as it relies on the density of the absorbing gas and the amount of XUV photons available at each altitude. Whereas the XUV heating rate per mass (Fig. A3, top left) is stronger in the upper thermosphere as it is normalized by the local density profile of the absorbing gas. While the characteristics of the XUV heating rate are identical across the four models, the absolute values of the heating rate are different between models. Models with a stronger eddy diffusion coefficient show a weaker XUV heating rate per unit mass, but the volumetric heating rate shows a more complex behaviour. At the upper thermosphere, the heating rate per unit volume is higher for models with stronger eddy diffusion coefficients, which can be attributed to the more efficient transport of heavier XUV-active molecules to higher altitudes. The volumetric XUV heating rate is also higher for the non-LTE models, which could be due to less effective cooling in these models leading to be a more expanded atmosphere. Both phenomena could also explain the opposite trend in the volumetric heating rate pxrofile at the lower thermosphere.

The chemical heating (bottom-left panels in Fig. A2 and A3) exhibits broadly similar behaviour to the XUV heating rate. Differences in the vertical distribution of chemical species between the four models could explain observed intermodel variations in the chemical heating rate. Our model treats the stellar IR spectrum as a blackbody of 5777 K and currently only considers IR absorption by CO_2 and H_2O. Since the abundance of these two absorbing molecules is negligible in Titan's thermosphere and also in our models, heating due to IR absorption is negligible. Both R. V. Yelle (1991) and D. Snowden and R. V. Yelle (2014) accounted for heating due to IR absorption in the CH_4 bands. A detailed investigation of the impact of IR absorption by CH_4 is beyond the scope of this work and will be left for the future, but its contribution towards the energy calculations is expected to be minor compared to XUV heating.

The total cooling rate in all four models is driven by the thermal emission of CH_4 and HCN. The volumetric cooling rates under the LTE assumption are derived from the cooling rate per molecule and the density profile of that molecule. As shown in the top-right panel of Fig. A2, the CH_4 volumetric cooling rates for our LTE models decrease in strength from Model B to A, showing a correlation with the adopted K_E profile. In Fig. A3, the CH_4 cooling per mass for the LTE models at the upper thermosphere does not exhibit any dependence on K_E. At the lower thermosphere, however, the CH_4 cooling rate per mass increases with an increase with K_E. The non-LTE models by construction

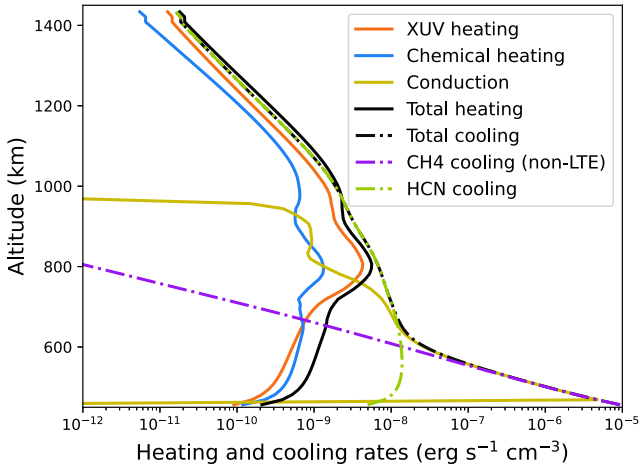


Figure A1. Total heating and cooling rates for Model A (non-LTE). The dominant heating and cooling functions are also shown by the coloured lines.

Downloaded from academic.oup.com/mnras/article/553/1/stag1951/8916626 by guest on 10 November 2026

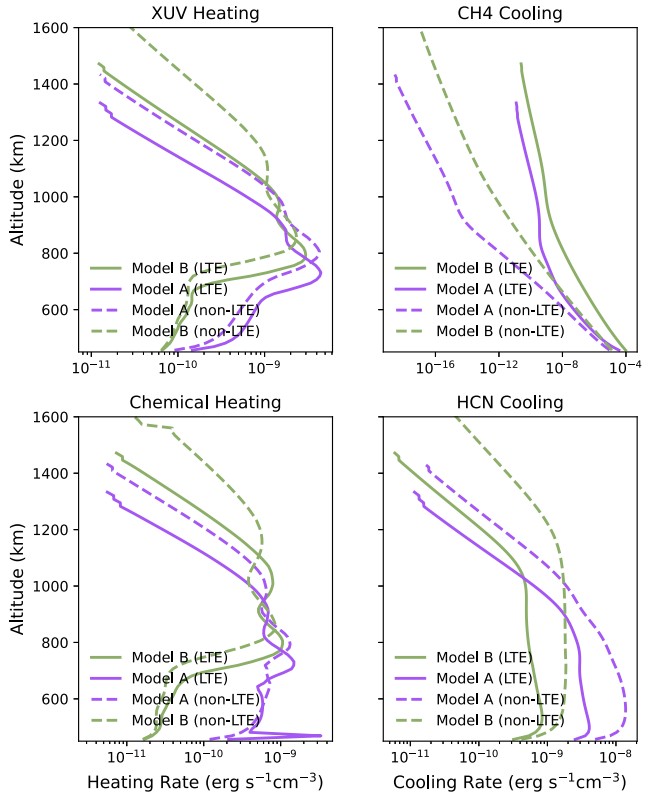


Figure A2. Heating (left panel) and cooling (right panel) rates in erg s^{-1} cm^{-3} versus altitude (km). The colour scheme is the same as in Fig. 1.

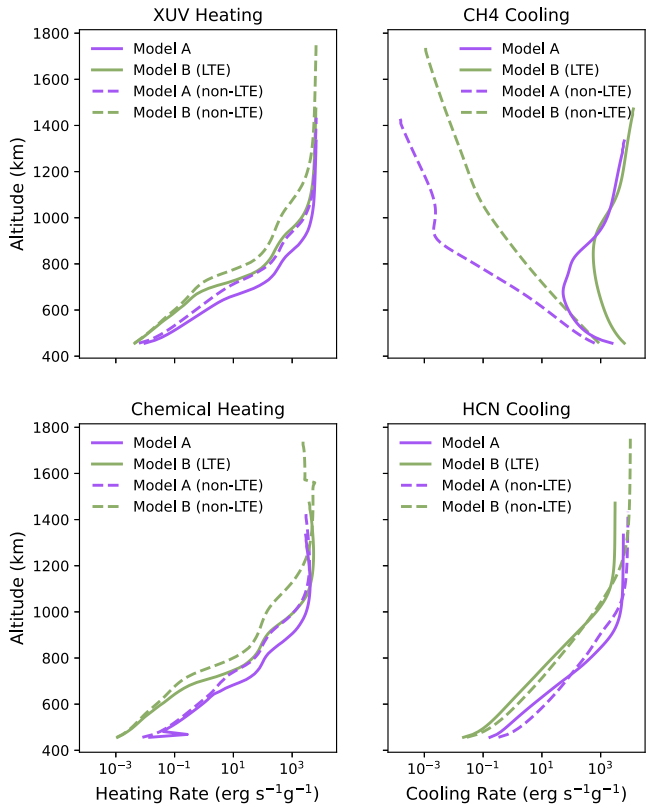


Figure A3. Heating (left panel) and cooling (right panel) rates in erg s^{-1} g^{-1} versus altitude (km). The colour scheme is the same as in Fig. 1.

have a weaker CH_4 cooling when compared to the LTE models, as departures from LTE reduces cooling efficiency. Between the two non-LTE models, CH_4 cooling is stronger for the model with a higher K_E.

The HCN cooling rate is calculated under the LTE assumption only. Any reference to a non-LTE model points towards non-LTE treatment of CH_4 cooling in that model. The bottom-right panels in Fig. A2 and A3 show the HCN cooling rates. The volumetric HCN cooling exhibits a more complex behaviour when compared to the HCN cooling per unit mass, which shows a consistently weaker HCN cooling profile with increase in K_E. At the lower thermosphere, the volumteric HCN cooling rate is weaker for the stronger K_E models, but at the upper thermosphere the cooling rate increases for the stronger K_E models. This is not surprising as HCN is a product of CH_4 and N_2 chemistry, and its density structure is strongly tied to the adopted K_E profile which impacts the volumteric cooling rate of this molecule. Finally, the volumetric cooling rate of the non-LTE models is stronger than the LTE models, which could be explained by the overall hotter and expanded atmosphere due to a less efficient CH_4 cooling in those models which impacts the production of HCN and consequently the HCN density in these models.

APPENDIX B: ENERGY DEPOSITION IN TITAN'S UPPER ATMOSPHERE OVER TIME

Fig. B1 shows the temporal evolution of the Solar XUV spectrum over time, from 0 Ga (present) to 3 Ga in the past, based on the model of M. W. Claire et al. (2012). At shorter wavelengths, the spectral irradiance of the young Sun is up to eight times higher than that of the present-day Sun, whereas this difference progressively decreases towards longer wavelengths. The attenuation of this solar XUV flux in Titan's upper atmosphere is strongly wavelength-dependent, with photons of different wavelengths being absorbed at different altitudes as the radiation propagates downward through the atmosphere, as illustrated in Fig. B2. While majority of the X-ray and far-UV flux gets absorbed above 800 km, a vast majority of the EUV flux gets absorbed above 1000 km. In contrast, the near-UV radiation at wavelengths longer than 1600 Å experiences negligible absorbtion in the upper atmosphere. Overall, the transmitted flux is highest for the youngest Sun, consistent with its enhanced incident XUV irradiance in Fig. B1. However, this trend shows a weak reversal in the near-UV, where the present-day Sun produces a slightly higher transmitted flux because its incident spectral irradiance exceeds that of the younger Sun at these wavelengths.

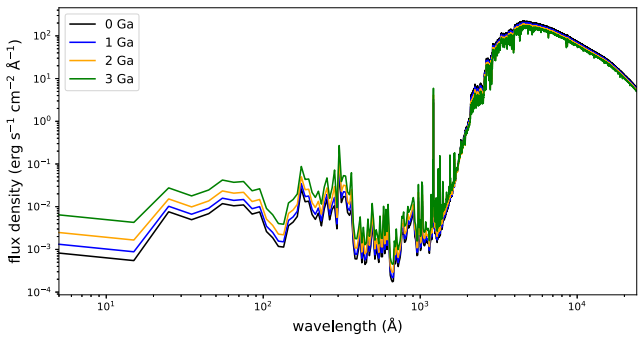


Figure B1. Solar X-ray and UV spectrum from the M. W. Claire et al. (2012) model over time, from 0 to 3 Ga in the past.

Downloaded from academic.oup.com/mnras/article/553/1/stag1951/8916626 by guest on 10 November 2026

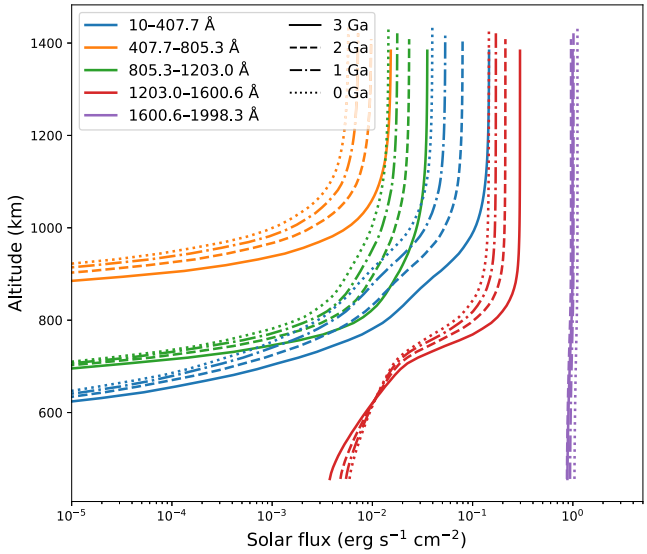


Figure B2. XUV flux transfer through Titan's upper atmospheric temporal models, from 0 to 3 Ga in the past (marked by the different line styles). The colours represent different wavelength bins, as listed in the legend.

APPENDIX C: CHEMICAL REACTIONS

Table C1. Photoreactions.

No.	Reaction	Ref.
R1	$CH_4 + h\nu \rightarrow CH_3 + H$	1
R2	$CH_4 + h\nu \rightarrow {}^1CH_2 + H_2$	1
R3	$CH_4 + h\nu \rightarrow CH_2 + H_2$	1
R4	$CH_4 + h\nu \rightarrow CH + H_2 + H$	1
R5	$C_2H_2 + h\nu \rightarrow C_2H + H$	1
R6	$C_2H_2 + h\nu \rightarrow C_2 + H_2$	1
R7	$C_2H_4 + h\nu \rightarrow C_2H_2 + H_2$	1
R8	$C_2H_4 + h\nu \rightarrow C_2H_2 + H + H$	1
R9	$C_2H_6 + h\nu \rightarrow C_2H_4 + H_2$	1
R10	$C_2H_6 + h\nu \rightarrow CH_4 + {}^1CH_2$	1
R11	$C_2H_6 + h\nu \rightarrow CH_3 + CH_3$	1
R12	$C_4H_2 + h\nu \rightarrow C_4H + H$	2
R13	$C_4H_2 + h\nu \rightarrow C_2H + C_2H$	2
R14	$C_4H_4 + h\nu \rightarrow C_4H_2 + H_2$	2
R15	$NH_3 + h\nu \rightarrow NH_2 + H$	1
R16	$NH_3 + h\nu \rightarrow NH + H + H$	1
R17	$HCN + h\nu \rightarrow H + CN$	1
R18	$HC_3N + h\nu \rightarrow C_2H + CN$	1
R19	$C_2N_2 + h\nu \rightarrow CN + CN$	2

Note. References: 1: W. Huebner & J. Mukherjee (2015); 2: H. Keller-Rudek et al. (2013).

Downloaded from academic.oup.com/mnras/article/553/1/stag1951/8916626 by guest on 10 November 2026

Table C2. Thermal reactions involving neutrals.

No.	Reaction	Energy eV	Temperature K	Rate constant (k_0)	Ref.
R1	$CH + CH_4 \longrightarrow C_2H_4 + H$	2.5	10–298	$1.6 \times 10^{-10} \left(\frac{T}{300}\right)^{-1.04} \exp\left(\frac{-36.1}{T}\right)$	
R2	$CH + CH_4 \longrightarrow CH_2 + CH_3$	−0.2	10–800	$2.28 \times 10^{-11} \left(\frac{T}{300}\right)^{0.7} \exp\left(\frac{-3000}{T}\right)$	1
R3	$^1CH_2 + CH_4 \longrightarrow CH_3 + CH_3$	0.65	43–498	$7.87 \times 10^{-11} \left(\frac{T}{300}\right)^{-0.467} \exp\left(\frac{-28.8}{T}\right)$	2
R4	$^1CH_2 + C_2H_4 \longrightarrow H + C_3H_5$	–	43–498	$1.88 \times 10^{-9} \left(\frac{T}{300}\right)^{-3.56} \exp\left(\frac{-724}{T}\right)$	
R5	$^1CH_2 + C_2H_5 \longrightarrow H + C_3H_6$	–	50–200	1.50×10^{-11}	
R6	$^1CH_2 + N_2 \longrightarrow CH_2 + N_2$	0.4	43–200	$6.00 \times 10^{-12} \left(\frac{T}{300}\right)^{-0.739}$	3
R7	$^1CH_2 + N_2 \longrightarrow CH_2 + N_2$	0.4	200–798	$6.55 \times 10^{-12} \left(\frac{T}{300}\right)^{1.17} \exp\left(\frac{-153}{T}\right)$	4
R8	$^1CH_2 + H_2 \longrightarrow CH_3 + H$	0.3	10–280	$5.0 \times 10^{-11} \exp\left(\frac{-4870}{T}\right)$	
R9	$CH_2 + CH_2 \longrightarrow C_2H_2 + H_2$	1.7	50–200	5.3×10^{-11}	5
R10	$CH_2 + CH_3 \longrightarrow C_2H_4 + H$	2.7	50–200	7.0×10^{-11}	2
R11	$CH_2 + CH_3 \longrightarrow C_2H_4 + H$	2.7	298–3000	1.2×10^{-10}	6
R12	$CH_3 + CH_3 + M \longrightarrow C_2H_6 + M$	3.8	50–200	$1.13 \times 10^{-25} \left(\frac{T}{300}\right)^{-3.75} \exp\left(\frac{-494}{T}\right)$	2
R13	$CH_3 + CH_3 + M \longrightarrow C_2H_6 + M$	3.8	300–2000	$1.6 \times 10^{-24} \left(\frac{T}{300}\right)^{-7.0} \exp\left(\frac{-1390}{T}\right)$	6
R14	$CH_3 + C_2H_3 \longrightarrow C_2H_2 + CH_4$	–	10–800	3.30×10^{-11}	
R15	$CH_3 + C_2H_4 \longrightarrow C_2H_3 + CH_4$	–	50–200	$1.61 \times 10^{-14} \left(\frac{T}{300}\right)^{3.7} \exp\left(\frac{-4780}{T}\right)$	
R16	$CH_3 + C_2H_5 \longrightarrow C_2H_4 + CH_4$	–	50–200	1.90×10^{-12}	
R17	$CH_3 + C_2H_5 \longrightarrow C_2H_4 + CH_4$	–	300–2000	1.50×10^{-12}	
R18	$CH_3 + C_2H_6 \longrightarrow C_2H_5 + CH_4$	–	50–200	$1.82 \times 10^{-16} \left(\frac{T}{300}\right)^{6} \exp\left(\frac{-3040}{T}\right)$	
R19	$CH_3 + C_2H_5 + M \longrightarrow C_3H_8 + M$	–	50–200	$1.05 \times 10^{-19} \left(\frac{T}{300}\right)^{-16.1} \exp\left(\frac{-1900}{T}\right)$	
R20	$CH_3 + C_3H_5 \longrightarrow CH_3C_2H + CH_4$	–	50–200	$4.03 \times 10^{-13} \left(\frac{T}{300}\right)^{-0.32} \exp\left(\frac{66}{T}\right)$	
R21	$CH_3 + C_3H_8 \longrightarrow C_3H_7 + CH_4$	–	50–200	$1.65 \times 10^{-15} \left(\frac{T_{\rm neut}}{300}\right)^{3.65} \exp\left(\frac{-3600}{T_{\rm neut}}\right)$	
R22	$CH_3 + C_4H_3 \longrightarrow C_4H_2 + CH_4$	–	50–200	3.0×10^{-11}	
R23	$CH_3 + C_4H_4 \longrightarrow C_4H_3 + CH_4$	–	50–200	$6.61 \times 10^{-13} \exp\left(\frac{-2500}{T}\right)$	
R24	$CH_3 + N \longrightarrow HCN + H_2$	5.07	10–300	$5.00 \times 10^{-11} \exp\left(\frac{-250}{T}\right)$	5
R25	$CH_3 + NH_2 \longrightarrow CH_4 + NH$	0.45	–	$4.65 \times 10^{-18} \left(\frac{T}{300}\right)^{1.94} \exp\left(\frac{-4635}{T}\right)$	7
R26	$CH_3 + NH_2 \longrightarrow NH_3 + CH_2$	−0.18	–	$2.66 \times 10^{-18} \left(\frac{T}{300}\right)^{1.87} \exp\left(-\frac{3810}{T}\right)$	7
R27	$CH_3 + NH_3 \longrightarrow NH_2 + CH_4$	–	50–200	$5.10 \times 10^{-14} \left(\frac{T}{300}\right)^{2.86} \exp\left(\frac{-7340}{T}\right)$	
R28	$CH_3 + H_2 \longrightarrow CH_4 + H$	–	50–200	$6.99 \times 10^{-14} \left(\frac{T}{300}\right)^{2.74} \exp\left(\frac{-4740}{T}\right)$	
R29	$C_2 + CH_4 \longrightarrow C_2H + CH_3$	0.4	50–200	$5.05 \times 10^{-11} \exp\left(\frac{-297}{T}\right)$	2
R30	$C_2 + H_2 \longrightarrow C_2H + H$	1.5	50–200	$1.77 \times 10^{-10} \exp\left(\frac{-1470}{T}\right)$	2
R31	$C_2H + CH_4 \longrightarrow C_2H_2 + CH_3$	1.2	150–780	$7.67 \times 10^{-12} \left(\frac{T}{300}\right)^{0.94} \exp\left(\frac{-328}{T}\right)$	6
R32	$C_2H + C_2H_6 \longrightarrow C_2H_2 + C_2H_5$	1.3	150–780	$3.33 \times 10^{-11} \left(\frac{T}{300}\right)^{-0.28} \exp\left(\frac{62}{T}\right)$	6
R33	$C_2H + C_2H_2 \longrightarrow C_4H_2 + H$	1.3	50–2700	1.3×10^{-10}	2, 6
R34	$C_2H + HCN \longrightarrow HC_3N + H$	1.2	50–200	$5.3 \times 10^{-12} \exp\left(\frac{-770}{T}\right)$	2
R35	$C_2H + H_2 \longrightarrow C_2H_2 + H$	1.3	180–300	$1.95 \times 10^{-12} \left(\frac{T}{300}\right)^{2.32} \exp\left(\frac{-444}{T}\right)$	6
R36	$C_2H + H_2 \longrightarrow C_2H_2 + H$	1.3	50–180	$1.2 \times 10^{-11} \exp\left(\frac{-998}{T}\right)$	2
R37	$C_2H_2 + H + M \longrightarrow C_2H_3 + M$	1.5	50–200	$3.3 \times 10^{-30} \exp\left(\frac{-740}{T}\right)$	2
R38	$C_2H_3 + H \longrightarrow C_2H_2 + H_2$	3.0	300	7.0×10^{-11}	6
R39	$C_2H_3 + H \longrightarrow C_2H_2 + H_2$	3.0	50–200	2.0×10^{-11}	2
R40	$C_2H_3 + C_2H_3 \longrightarrow C_2H_2 + C_2H_4$	0.1	50–200	3.5×10^{-11}	2
R41	$C_2H_4 + H + M \longrightarrow C_2H_5 + M$	1.4	50–200	$1.39 \times 10^{-29} \exp\left(\frac{-562}{T}\right)$	2
R42	$C_2H_4 + H + M \longrightarrow C_2H_5 + M$	1.4	300–800	$1.30 \times 10^{-29} \exp\left(\frac{-380}{T}\right)$	6
R43	$C_2H_5 + H \longrightarrow C_2H_4 + H_2$	2.9	10–300	3.0×10^{-12}	8
R44	$C_2H_5 + H \longrightarrow C_2H_4 + H_2$	2.9	300–2000	7.0×10^{-11}	6
R45	$C_2H_5 + H \longrightarrow CH_3 + CH_3$	1.9	10–300	5.99×10^{-11}	8
R46	$CH_3C_2H + H + M \longrightarrow CH_3 + C_2H_2 + M$	2.3	50–200	$8.89 \times 10^{-29} \left(\frac{T}{300}\right)^{-2.0} \exp\left(\frac{-1220}{T}\right)$	2
R47	$C_4H + CH_4 \longrightarrow C_4H_2 + CH_3$	1.0	300–1000	$2.98 \times 10^{-13} \left(\frac{T}{300}\right)^{2.72} \exp\left(\frac{-371}{T}\right)$	9
R48	$C_4H + CH_4 \longrightarrow C_4H_2 + CH_3$	1.0	50–200	$1.7 \times 10^{-12} \exp\left(\frac{-619}{T}\right)$	2
R49	$C_4H + CH_4 \longrightarrow C_4H_2 + CH_3$	1.0	200–300	$1.6 \times 10^{-11} \exp\left(\frac{-610}{T}\right)$	10
R50	$C_4H + CH_4 \longrightarrow C_4H_2 + CH_3$	1.0	300–1000	$2.98 \times 10^{-13} \left(\frac{T}{300}\right)^{2.72} \exp\left(\frac{-371}{T}\right)$	9
R51	$C_4H + C_2H_6 \longrightarrow C_4H_2 + C_2H_5$	1.1	50–200	$2.87 \times 10^{-11} \left(\frac{T}{300}\right)^{-1.24} \exp\left(\frac{-25.6}{T}\right)$	2

Downloaded from academic.oup.com/mnras/article/553/1/stag1951/8916626 by guest on 10 November 2026

Table C2 – *continued*

No.	Reaction	Energy eV	Temperature K	Rate constant (k_0)	Ref.
R52	$C_4H_2 + H + M \longrightarrow C_4H_3 + M$	1.3	50–200	$3.30 \times 10^{-30} \exp\left(\frac{-740}{T}\right)$	2
R53	$C_4H_3 + H \longrightarrow C_2H_2 + C_2H_2$	5.5	50–200	3.3×10^{-12}	2
R54	$C_4H_3 + H \longrightarrow H_2 + C_4H_2$	3.2	10–800	8.3×10^{-11}	1
R55	$C_4H_3 + H \longrightarrow C_4H_4$	4.8	50–200	$3.47 \times 10^{-27} \left(\frac{T}{300}\right)^{-1.3}$	
R56	$CN + CH_4 \longrightarrow HCN + CH_3$	0.9	10–160	$5.73 \times 10^{-12} \exp\left(\frac{-675}{T}\right)$	2
R57	$CN + CH_4 \longrightarrow HCN + CH_3$	0.9	160–1500	$6.2 \times 10^{-12} \exp\left(\frac{-735}{T}\right)$	6
R58	$CN + C_2H_2 \longrightarrow H + HC_3N$	0.9	50–200	$2.71 \times 10^{-10} \left(\frac{T}{300}\right)^{-0.52} \exp\left(\frac{-20}{T}\right)$	2
R59	$CN + HCN \longrightarrow C_2N_2 + H$	0.5	50–200	$4.3 \times 10^{-13} \left(\frac{T}{300}\right)^{1.71} \exp\left(\frac{-770}{T}\right)$	2
R60	$HC_2N_2 + H \longrightarrow HCN + HCN$	–	50–200	$1.7 \times 10^{-13} \exp\left(\frac{-110}{T}\right)$	2
R61	$H_2C_3N + H \longrightarrow HCN + C_2H_2$	3.1	50–200	1.5×10^{-11}	
R62	$HC_3N + H + M \longrightarrow H_2C_3N + M$	1.4	50–200	$4.19 \times 10^{-36} \exp\left(\frac{-740}{T}\right) n_{\rm tot}$	2
R63	$N(2D) + CH_4 \longrightarrow NH + CH_3$	–	50–200	$1.60 \times 10^{-10} \exp\left(\frac{-267}{T}\right)$	11, 2
R64	$N(2D) + NH_3 \longrightarrow NH + NH_2$	–	200–300	5.00×10^{-11}	7, 11
R65	$N + NH_3 \longrightarrow N_2H + H_2$	–	710–930	$7.42 \times 10^{-12} \exp\left(-\frac{4830}{T}\right)$	7
R66	$NH + N \longrightarrow N_2 + H$	6.4	10–500	$5.00 \times 10^{-11} \left(\frac{T}{300}\right)^{0.1}$	
R67	$NH + NH_2 \longrightarrow N_2H_2 + H$	1.14	200–2500	$6.98 \times 10^{-10} \left(\frac{T}{300}\right)^{-0.27} \exp\left(\frac{39}{T}\right)$	12
R68	$NH + NH_2 \longrightarrow NH_3 + N$	1.18	–	$1.59 \times 10^{-20} \left(\frac{T}{300}\right)^{2.46} \exp\left(-\frac{54}{T}\right)$	12
R69	$NH + N_2H_2 \longrightarrow NH_2 + N_2H$	–	300–2000	$4.00 \times 10^{-18} \left(\frac{T}{300}\right)^{2.0} \exp\left(\frac{600}{T}\right)$	7
R70	$NH + H_2CN \longrightarrow HCN + NH_2$	–	–	3.0×10^{-11}	7
R71	$NH_2 + CH_4 \longrightarrow CH_3 + NH_3$	0.08	300–2000	$7.80 \times 10^{-12} \exp\left(-\frac{4680}{T}\right)$	7
R72	$NH_2 + C_2H \longrightarrow NH + C_2H_2$	0.76	–	4.00×10^{-11}	7
R73	$NH_2 + C_2H_3 \longrightarrow NH_3 + C_2H_2$	3.1	–	5.00×10^{-11}	7
R74	$NH_2 + C_2H_4 \longrightarrow NH_3 + C_2H_3$	−0.18	1640–1940	$8.80 \times 10^{-12} \exp\left(\frac{-5170}{T}\right)$	7
R75	$NH_2 + C_2H_5 \longrightarrow NH_3 + C_2H_4$	3.06	–	3.15×10^{-11}	7
R76	$NH_2 + C_2H_6 \longrightarrow NH_3 + C_2H_5$	0.24	1500–2100	$1.61 \times 10^{-11} \exp\left(-\frac{5770}{T}\right)$	7
R77	$NH_2 + H_2 \longrightarrow NH_3 + H$	0.10	400–2200	$2.49 \times 10^{-20} \left(\frac{T}{300}\right)^{2.6} \exp\left(-\frac{3007}{T}\right)$	7
R78	$NH_2 + H_2CN \longrightarrow NH_3 + HCN$	–	–	$2.29 \times 10^{-8} \left(\frac{T}{300}\right)^{-1.06} \exp\left(-\frac{60.8}{T}\right)$	13
R79	$NH_2 + NH_2 \longrightarrow NH_3 + NH$	0.53	300–2500	$9.35 \times 10^{-24} \left(\frac{T}{300}\right)^{3.53} \exp\left(-\frac{278}{T}\right)$	7
R80	$NH_2 + NH_2 \longrightarrow N_2H_2 + H_2$	1.57	500–2250	$2.89 \times 10^{-16} \left(\frac{T}{300}\right)^{1.02} \exp\left(-\frac{5930}{T}\right)$	7
R81	$NH_2 + N_2H_2 \longrightarrow NH_3 + N_2H$	–	300–2000	$3.0 \times 10^{-18} \left(\frac{T}{300}\right)^{1.94} \exp\left(\frac{580}{T}\right)$	7
R82	$NH_2 + N_2H_3 \longrightarrow NH_3 + N_2H_2$	–	600–2500	$1.53 \times 10^{-18} \left(\frac{T}{300}\right)^{1.94} \exp\left(\frac{580}{T}\right)$	7
R83	$NH_2 + NO \longrightarrow N_2H + OH$	–	400–1900	$7.28 \times 10^{-14} \left(\frac{T}{300}\right)^{0.29} \exp\left(\frac{438}{T}\right)$	7
R84	$NH_2 + NO_2 \longrightarrow N_2O + H_2O$	3.89	300–910	$2.56 \times 10^{-8} \left(\frac{T}{300}\right)^{-1.44} \exp\left(-\frac{135}{T}\right)$	7
R85	$NH_2 + O \longrightarrow H_2 + NO$	3.52	298–3000	8.30×10^{-12}	7
R86	$NH_2 + O_3 \longrightarrow H_2O + NO_2$	5.51	200–300	$4.30 \times 10^{-12} \exp\left(-\frac{930}{T}\right)$	7
R87	$NH_2 + OH \longrightarrow H_2O + NH$	1.06	250–3000	$1.49 \times 10^{-16} \left(\frac{T}{300}\right)^{1.5} \exp\left(\frac{230}{T}\right)$	7
R88	$NH_3 + CH \longrightarrow NH_2 + CH_2$	−0.26	300–1300	$7.24 \times 10^{-11} \exp\left(\frac{317}{T}\right)$	7
R89	$NH_3 + CN \longrightarrow HCN + NH_2$	0.76	294–761	$1.52 \times 10^{-11} \exp\left(\frac{180}{T}\right)$	7
R90	$NH_3 + OH \longrightarrow NH_2 + H_2O$	0.53	300–2000	$7.49 \times 10^{-14} \left(\frac{T}{300}\right)^{0.56} \exp\left(-\frac{730}{T}\right)$	14
R91	$N_2H + NH_2 \longrightarrow N_2 + NH_3$	–	–	$1.53 \times 10^{-18} \left(\frac{T}{300}\right)^{1.94} \exp\left(\frac{580}{T}\right)$	7
R92	$N_2H_2 + CH_3 \longrightarrow N_2H + CH_4$	–	300–2000	$2.66 \times 10^{-18} \left(\frac{T}{300}\right)^{1.87} \exp\left(-\frac{1495}{T}\right)$	7
R93	$N_2H_2 + H \longrightarrow N_2H + H_2$	–	300–2000	$7.97 \times 10^{-16} \left(\frac{T}{300}\right)^{1.5} \exp\left(-\frac{795}{T}\right)$	7
R94	$N_2H_2 + O \longrightarrow N_2H + OH$	–	300–2000	$5.50 \times 10^{-16} \left(\frac{T}{300}\right)^{1.5} \exp\left(-\frac{250}{T}\right)$	7
R95	$N_2H_2 + OH \longrightarrow N_2H + H_2O$	–	300–2000	$4.00 \times 10^{-18} \left(\frac{T}{300}\right)^{2.0} \exp\left(\frac{600}{T}\right)$	7
R96	$N_2H_3 + NH \longrightarrow N_2H_2 + NH_2$	–	–	2.70×10^{-12}	
R97	$NO + NH_2 \longrightarrow N_2 + H_2O$	5.34	300–2000	$7.90 \times 10^{-9} \left(\frac{T}{300}\right)^{-1.1} \exp\left(-\frac{98}{T}\right)$	7
R98	$H + NH_2 + M \longrightarrow NH_3 + M$	4.62	1–1000	$5.38 \times 10^{-25} \left(\frac{T}{300}\right)^{-2.0}$	7, 15
R99	$H + HCN + M \longrightarrow H_2CN + M$	1.1	50–200	$3.3 \times 10^{-30} \left(\frac{T}{300}\right)^{-2.73} \exp\left(\frac{-3860}{T}\right)$	2
R100	$H + H_2CN \longrightarrow H_2 + HCN$	3.4	10–300	6.0×10^{-11}	8
R101	$H + C_2N_2 + M \longrightarrow HCN_2 + M$	–	50–200	$1.0 \times 10^{-28} \exp\left(\frac{-740}{T}\right)$	2

Downloaded from academic.oup.com/mnras/article/553/1/stag1951/8916626 by guest on 10 November 2026

Table C2 – *continued*

No.	Reaction	Energy eV	Temperature K	Rate constant (k_0)	Ref.
R102	$H_2 + N + M \longrightarrow NH_2 + M$	3.01	1–1000	1.0×10^{-36}	7
R103	$HO_2 + NH_2 \longrightarrow NH_3 + O_2$	2.38	300–2000	$2.75 \times 10^{-20} \left(\frac{T}{300}\right)^{1.55} \exp\left(-\frac{1020}{T}\right)$	7, 16
R104	$O + NH_3 \longrightarrow OH + NH_2$	−0.17	500–2500	$1.60 \times 10^{-11} \exp\left(-\frac{3670}{T}\right)$	7
R105	$OH + CH_3 \longrightarrow {}^1CH_2 + H_2O$	–	150–1200	$1.0 \times 10^{-10} \left(\frac{T}{300}\right)^{-0.91} \exp\left(\frac{-275}{T}\right)$	7
R106	$OH + CH_3 \longrightarrow CH_3O + H$	–	298–2000	$2.0 \times 10^{-14} \exp\left(\frac{-6990}{T}\right)$	6
R107	$OH + CH_3 \longrightarrow CH_2OH + H$	–	298–2000	$1.2 \times 10^{-12} \exp\left(\frac{-2760}{T}\right)$	6
R108	$OH + CH_3 \longrightarrow H_2 + H_2CO$	–	298–2000	$5.3 \times 10^{-15} \exp\left(\frac{-2760}{T}\right)$	6
R109	$OH + NH \longrightarrow O + NH_2$	−0.36	298–3000	$1.66 \times 10^{-12} \left(\frac{T}{300}\right)^{0.1} \exp\left(\frac{-5800}{T}\right)$	7
R110	$OH + NH \longrightarrow O + NH_2$	−0.36	298–3000	$1.66 \times 10^{-12} \left(\frac{T}{300}\right)^{0.1} \exp\left(\frac{-5800}{T}\right)$	7
R111	$OH + HCN \longrightarrow NH_2 + CO$	0.99	500–2500	$1.07 \times 10^{-13} \exp\left(-\frac{5890}{T}\right)$	7
R112	$H_2O + CH_3 \longrightarrow CH_4 + OH$	–	50–200	$1.22 \times 10^{-14} \left(\frac{T}{300}\right)^{2.9} \exp\left(\frac{-7480}{T}\right)$	
R113	$HCO + CH_3 \longrightarrow CO + CH_4$	–	50–200	2.01×10^{-10}	
R114	$H_2CO + CH_3 \longrightarrow CH_4 + HCO$	–	50–200	$6.79 \times 10^{-12} \exp\left(\frac{-4450}{T}\right)$	
R115	$H_2CO + CH_3 \longrightarrow CH_4 + HCO$	–	300–2000	$1.12 \times 10^{-14} \left(\frac{T}{300}\right)^{3.36} \exp\left(\frac{-2170}{T}\right)$	
R116	$CH_3O + CH_3 \longrightarrow H_2CO + CH_4$	–	50–200	4.00×10^{-11}	
R117	$CH_2OH + CH_3 \longrightarrow H_2CO + CH_4$	–	50–200	4.00×10^{-12}	

Note. References: Reaction network based on the chemical scheme of Y. L. Yung et al. (1984). The temperature ranges and rate constants are taken from KIDA (V. Wakelam et al. 2012). The formation enthalpy values used to calculate the reaction energies are taken from the Argonne Active Thermochemical Tables (B. Ruscic & D. Bross 2022) and NIST (P. J. Linstrom & W. G. Mallard 2001). For reactions involving a third body, the Modified Arrenhius equation for the low pressure condition is multiplied by the total number density of the gas. If any data are taken from other resources they are listed in the reference column. 1: N. Harada & E. Herbst 2008; 2: E. Hébrard et al. 2009; 3: K. Douglas et al. 2018; 4: K. L. Gannon et al. 2010; 5: Y. L. Yung et al. 1984; 6: D. L. Baulch et al. 2005; 7: S.-M. Tsai et al. 2021; 8: J.-C. Loison, V. Wakelam & K. M. Hickson 2014; 9: R.-P. Huo et al. 2011; 10: C. Berteloite et al. 2010; 11: J. T. Herron 1999; 12: S. J. Klippenstein et al. 2009; 13: R. V. Yelle et al. 2010; 14: V. Samu et al. 2018; 15: P. B. Pagsberg, J. Eriksen & H. C. Christensen 1979; 16: R. Sumathi & S. Peyerimhoff 1996.

This paper has been typeset from a TEX/LATEX file prepared by the author.

Downloaded from academic.oup.com/mnras/article/553/1/stag1951/8916626 by guest on 10 November 2026

© The Author(s) 2026.
Published by Oxford University Press on behalf of Royal Astronomical Society. This is an Open Access article distributed under the terms of the Creative Commons Attribution License (https://creativecommons.org/licenses/by/4.0/), which permits unrestricted reuse, distribution, and reproduction in any medium, provided the original work is properly cited.